Local Wavelet Pattern based Glaucoma Detection from Fundus Images

M.Tech. Thesis

By

MOHNISH BELANI

DEPARTMENT OF ELECTRICAL ENGINEERING

INDIAN INSTITUTE OF TECHNOLOGY INDORE

JUNE 2022

Local Wavelet Pattern based Glaucoma Detection from Fundus Images

A THESIS

Submitted in partial fulfillment of the requirements for the award of the degree

of

Master of Technology

by

MOHNISH BELANI

DEPARTMENT OF ELECTRICAL ENGINEERING

INDIAN INSTITUTE OF TECHNOLOGY INDORE

JUNE 2022

INDIAN INSTITUTE OF TECHNOLOGY INDORE

CANDIDATE'S DECLARATION

I hereby certify that the work which is being presented in the thesis entitled **Local Wavelet Pattern based Glaucoma Detection from Fundus Images** in the partial fulfillment of the requirements for the award of the degree of **Master of Technology** and submitted in the **Department of Electrical Engineering, Indian Institute of Technology Indore**, is an authentic record of my own work carried out during the time period from July 2021 to May 2022 under the supervision of Professor Ram Bilas Pachori.

The matter presented in this thesis has not been submitted by me for the award of any other degree of this or any other institute.

MBelani

01/06/2022

Signature of the student with date
MOHNISH BELANI

This is to certify that the above statement made by the candidate is correct to the best of my/our knowledge.

08.06.2022

Signature of the Supervisor of
M.Tech. thesis (with date)
Professor Ram Bilas Pachori

Mohnish Belani has successfully given his/her M.Tech. Oral Examination held on 06.06.2022

Signature(s) of Supervisor(s) of M.Tech. thesis
Date: 08.06.2022

Convener, DPGC (Dr. Swaminathan R.)
Date: 08/06/2022

06.06.2022
Signature of PSPC Member #2
(Dr. Vimal Bhatia)
Date:

Signature of PSPC Member #2
(Dr. Anirban Sengupta)
Date: 08.06.2022

Acknowledgments

Firstly, I would like to convey my sincere gratitude to my supervisor Professor Ram Bilas Pachori for his continuous support and valuable guidance. His guidance helped me in throughout my work. I have been able to push myself beyond my expectations with his excellent supervision and encouragement.

I would like to thank my Post Graduate Student Progress Committee (PSPC) members Professor Vimal Bhatia and Associate Professor Anirban Sengupta for their insightful comments and suggestions towards my research.

I sincerely acknowledge Indian Institute of Technology Indore and Ministry of Human Resource Development (MHRD) for supporting my M.Tech. by providing lab facilities and Teaching Assistant (TA) scholarship, respectively. Also, I would like to thank my Signal Analysis and Research (SARL) lab members Pradeep Chaudhary, Vivek Kumar Singh, Kritiprasanna Das, Makam Kiran Kumar, Shailesh Bhalerao, Aditya Nalwaya, and Ashok Mahato for their constant support and guidance throughout the thesis work.

Last but not least, my work would not have been possible without the encouragement of my parents, whose tremendous support helped me stay positive and overcome the worst of hurdles. To them, I will forever be grateful.

Abstract

An image descriptor known as the local wavelet pattern (LWP) is presented in this thesis to characterize retinal fundus images for glaucoma detection. The LWP is obtained for every pixel of the fundus image by encoding the relationship of the center pixel with the wavelet decomposed local neighbors. Another similar local image descriptor known as the local binary pattern (LBP) only takes into account the association of the center pixel with its surrounding pixels.

In the presented technique, the correspondence among the neighboring pixels is first established using wavelet decomposition and then its association with the transformed center pixel is considered. In order to range match the wavelet decomposed local neighbors and the center pixel, a center pixel transformation method is introduced.

This thesis studies: a) encoding the information between local neighboring pixels using wavelet analysis and b) calculating LWP using local wavelet decomposed vector and transformed center pixel vector. The LWP method is tested over two retinal fundus image databases for classification accuracy. We also weighed up the proposed LWP method with other local image descriptors, and the results suggest that LWP is far superior for retinal fundus image classification.

Contents

List of Figures

Chapter 1

Introduction

1.1 Glaucoma - the disease

The human vision is the most used among the five senses of the human body and the eye perceives most of the information around us [1]. A large portion of the human brain is used in processing visual information. The retina converts the incoming light signal into a neural signal suitable for it to be processed by the brain and it is a layered tissue lining the interior of the eye [2]. Sensation of vision to the human eye, which includes perception of depth and color differentiation is provided by rods and cones (also known as photoreceptors) in the retina [3]. The optic nerves is a grouping of approximately one million nerve fibers present in the retina. The beginning of the optic nerves in the retina is called the optic nerve head (ONH) or optic disc (OD), which is circular in shape and visibly bright in the fundus images.

Glaucoma damages the optic nerve (or retina) and is a group of chronic eye diseases that result in vision loss [4]. Open-angle (wide angle, chronic simple) glaucoma is the most common type of glaucoma, in which the drainage angle for fluid within the eye stays open, while closed-angle (narrow angle, acute congestive) glaucoma and normal-tension glaucoma are less prevalent. If left untreated, peripheral vision may continue to deteriorate, followed by central vision, eventually leading to blindness. The onset of closed-angle glaucoma might be gradual or abrupt. Severe eye pain, blurred vision, a mid-dilated pupil, redness of the eye, and nausea are all possible symptoms of an unexpected presentation. Once glaucoma has taken hold, vision loss is irreversible. Eyes affected by glaucoma are referred to as being glaucomatous. Glaucoma is caused by an increase in age, high eye pressure, a family history of glaucoma, and the use of steroid medication. A threshold of 21 mmHg or 2.8 kPa over atmospheric pressure (760 mmHg) is commonly used for eye pressures, with higher pressures posing a higher risk. In recent investigations, a big OD has been proposed as a risk factor for glaucoma [5]. A dilated eye examination is used to make the diagnosis. The optic nerve frequently exhibits an inappropriate amount of cupping. Globally, 64.3 million people (aged 40 to 80 years) were predicted to have glaucoma in 2013, rising to 76.0 million in 2020 and 111.8 million in 2040 [6][7].

Very often the glaucoma disease progresses quietly in the early stages and therefore it is also named as the 'sneak thief of sight'. The number of people affected has been increasing and patients are seldom aware of the disease, which can cause delay in the treatment.

1.2 Motivation

With the swift development of digital imaging and computer vision the prospect of using image processing techniques in ophthalmology has risen enormously. Image processing systems are used in standard clinical practices with the advancement of medical diagnostic systems. Vital information about the health of the sensory part of the visual system can be obtained from the retinal images. Many retinal diseases, such as glaucoma, age-related macular degeneration, diabetic retinopathy, retinopathy of prematurity, and Stargardt's disease can lead to permanent vision loss [8] [9]. These retinal diseases manifest as artifacts in the retinal image. Standardized large-scale screening can be provided using an automated system at a lower cost, which may reduce human errors, provide services to distant areas, as well as free from observer prejudice and tiredness. The major emphasis is on digital imaging of the retinal fundus, due to its low cost, high quality, speed, ease of archival, flexible visualization, retrieval, and transmission [10].

Heidelberg retinal tomography, scanning laser polarimetry, and optical coherence tomography are some of the scanning methods available for glaucoma. However these methods are expensive and necessitate experienced clinicians in order to use the equipment. The main challenge lies in finding a low-cost method with high accuracy that can be applied to large populations in a timely manner to identify those who are at risk at an early stage of the disease.

1.3 Major contributions

The entire algorithm for local wavelet pattern (LWP) image descriptor has been developed from scratch. We have varied the parameters of the algorithm to incorporate 30 different combinations and have performed the simulations for each case. Also the proposed method is applied to two publicly available datasets in order to obtain better insights in the inner workings of the algorithm. We have used two other local image descriptors to compare the results with our proposed method.

1.4 Organization of the thesis

The rest of this thesis is organized as follows: In Chapter 2, the literature survey consisting of different state of the art techniques for automated glaucoma detection is presented. Further, in Chapter 3, the proposed method i.e. the local wavelet transform technique along with the system model is discussed. Chapter 4 presents the simulation cases, results, and discussion in depth. Finally, Chapter 5 includes the conclusion and scope of the future work of this thesis.

Chapter 2

Literature Survey

2.1 Introduction

Having discussed the glaucoma disease and motivation for this thesis project in the previous chapter, let us now bring to light some of the state-of-the-art techniques/algorithms used for the automated detection of glaucoma present in literature.

Chaudhary et al. [11] [12] proposed a two-dimensional Fourier-Bessel series expansion empirical wavelet transform (2D-FBSE-EWT) used to decompose fundal retinal images into sub-images. Features such as chip histogram, gray level co-occurrence matrix and moment invariance are extracted from these sub-images and fed to various machine learning classifiers as well as ResNet - 50 convolutional neural network to obtain best accuracies of 98.21% and 94.30% respectively. Three features namely, the cup to disc ratio, the position of the optic disc center and the area of the blood vessels are used for the computer aided detection of glaucoma by Nayak et al. [13] [14] with an average classification rate of 90% using an artificial neural network (ANN) classifier. Calculation of glaucoma risk index (GRI) using image preprocessing, feature extraction and a two stage support vector machine (SVM) based classifier is proposed by Bock et al. [15] with an accuracy of 80%. Application of Radon transform and extraction of higher order statistical features followed by a Nave Bayesian classifier is proposed by Noronha et al. [16] [17] with a sensitivity of 100%. Various features such as mean, variance, energy, kurtosis etc. are extracted from Gabor transform and applied to fundus images and classified using SVM classifier yielding an accuracy of 93.10% is suggested by Acharya et al. [18]. Energy features are extracted by applying Radon transform on the segmented optical disc (part of fundus image) and then classified by SVM classifier. This technique achieves an accuracy of 97% and is proposed by Raghavendra et al. [19]. Features such as Kapoor entropy, Renyi entropy, Yager entropy etc. are extracted from 2-D iterative variational mode decomposition (VMD) coefficients and given to a least squares SVM (LS-SVM) classifier for classification. This method is developed by Maheshwari et al. [20] and achieves an accuracy of 95.19%. Trispectrum and complex wavelet features are extracted after optical disk segmented fundus image. These features then act as input to a neural network classifier yielding an accuracy of 81%. This technique was proposed by Raja et al. [21] [22]. Raja et al. [21] has also proposed decomposition techniques such as wavelet packet decomposition (WPD) [23] and optimal hyper analytic wavelet transform (OHAWT) [24]–[29] with corresponding accuracies of 85% and 96.2% respectively. Automated diagnosis of glaucoma using empirical wavelet transform (EWT) from digital fundus images is proposed by Maheshwari et al. [30] [31] [32]. The EWT decomposes the image into sub-images and correntropy features are extracted from these sub-images. A classification accuracy of 98.33% is achieved by the proposed technique using the LS-SVM classifier with various basis functions. Glaucoma identification based on anisotropic dual-tree complex wavelet transform and cup to disc ratio (CDR) features is presented by Kausu et al. [33] [34] [35]. These features are extracted from optic disk and optic cup segmented regions. An accuracy rate of 97.67% is attained by the proposed method using multilayer perceptron classifier. Nonlinear higher order statistics (HOS) based method for automated glaucoma detection is proposed by Sharma et al. [36].Various features are extracted from the diagonal of central slices of bispectrum and bicepstrum as applied to fundus images. The features are then fed to the SVM classifier yielding an accuracy of 98.8% and 95% using two databases. A bit-plane slicing (BPS) and local binary pattern (LBP) based novel approach for glaucoma diagnosis is proposed by Maheshwari et al. [37] [38]. The method first separates the red (R), green (G), and blue (B) channels from the input color fundus image and splits the channels into bit planes. Then local binary pattern (LBP) based statistical features are extracted from each of the bit planes of the individual channels. Finally these features are fed separately to three different SVMs for classification attaining an accuracy of 99.30% using 10-fold cross validation. Agrawal et al. [39] [40] [41] presents a unique method for automated glaucoma identification from digital fundus images using quasi-bivariate variational mode decomposition (QB-VMD). Seventy features are extracted from QB-VMD sub-band images. Accuracies of 85.94% and 86.13% are obtained using three-fold and ten-fold cross validation respectively by feeding these features to an LS-SVM classifier.

Recently we can observe the prevalence of many deep learning (DL) algorithms for medical image diagnosis. The only requirement for DL algorithms is that they require a massive dataset [42] for training the models and obtaining a higher classification accuracy. Also there is no need for feature selection while using these algorithms. Gulshan et al. [43] proposed a DL-based method for automated identification of diabetic retinopathy and diabetic macular edoema in retinal fundus images. The network used in this study is a convolutional neural network (CNN) based on the Inception-v3 architecture. A deep CNN for feature learning is used on fundus images to discriminate between glaucoma and non-glaucoma pattern. The method is proposed by Chen et al. [44] and the adopted network embeds micro neural networks (multilayer perceptron) with more complex structures to abstract the data within the receptive field. The work proposed by Orlando et al. [45] [46] uses two different CNNs, namely OverFeat and VGG-S, were applied to fundus images to generate feature vectors. Within this framework preprocessing techniques such as contrast-limited adaptive histogram equalization (CLAHE), vessel inpainting or cropping around the optic nerve head (ONH) area were explored to evaluate the improvement in feature discrimination. Three important, but previously understudied factors of employing deep convolutional neural networks to computer-aided detection problems are explored in the work by Shin et al. [47]. Also the usefulness of transfer learning from pre-trained ImageNet (via fine-tuning) is examined. An interpretable computer-aided diagnosis (CAD) pipeline for glaucoma detection using fundus images and run offline in mobile devices is proposed by Martins et al. [48]. In this work CNNs are used to perform segmentation and classification tasks.

2.2 Database

We have used two publicly available retinal fundus image databases in our proposed algorithm in order to test it thoroughly. It is made publicly available by the Medical Imaging Research Group of the University of La Laguna. It is named as an open retinal image database for optic nerve evaluation (RIM-ONE) [49] and is peculiarly designed for glaucoma diagnosis. This database has been developed with the help of three hospitals namely, Hospital Universitario Miguel Servet, Hospital Clínico San Carlos and Hospital Universitario de Canarias.

The first release of the RIM-ONE database RIM-ONE r1 consists of 169 high-resolution full fundus images of different subjects. 118 of these are normal eye images and 51 are images of glaucomatous eye. Figure 2.1 shows sample images from this database.

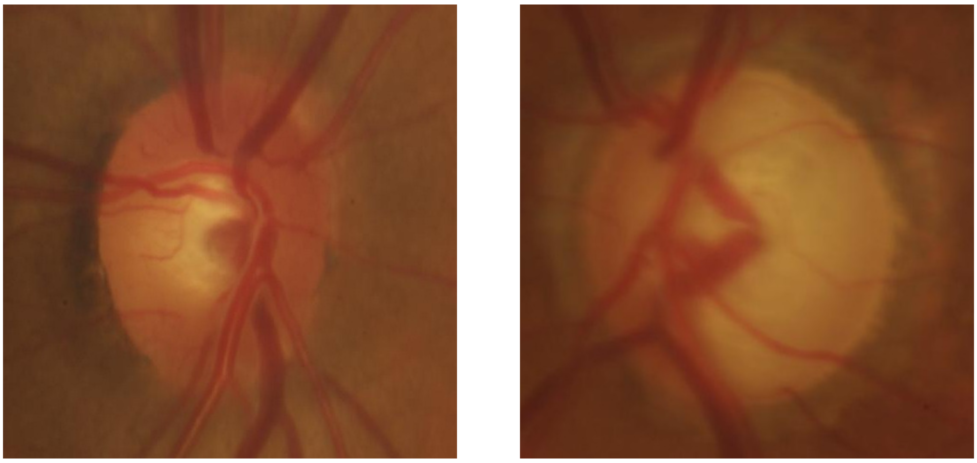

(a) Normal eye (b) Glaucomatous eye

Figure 2.1: Sample r1 database fundus images

The second release of the RIM-ONE database RIM-ONE r2 consists of 455 high-resolution full fundus images of different subjects. 255 of these are normal eye images and 200 are images of glaucomatous eye. Figure 2.2 shows sample images from this database.

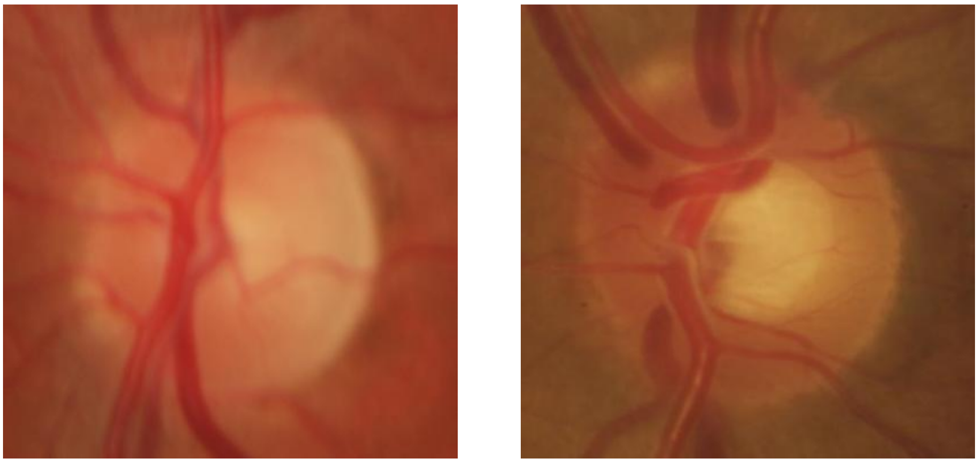

(a) Normal eye (b) Glaucomatous eye

Figure 2.2: Sample r2 database fundus images

Both the databases provide accurate gold standards of the optic nerve head (ONH) which is key to detecting glaucoma. It also serves well to designers of segmentation algorithms. These datasets are freely available for download at `http://medimrg.webs.ull.es/research/downloads/`.

Chapter 3

Proposed Method

3.1 Introduction

We have seen the various techniques that have been employed in order to automate the medical diagnosis process in the previous chapter. In this section, we will explain the overall framework for automating glaucoma detection using the local wavelet pattern (LWP) [50] image descriptor as well as the various steps involved in the formation of the feature matrix. An image descriptor is an algorithm which takes an image and outputs feature vectors. It is very useful since the most important information present in the image is captured by the feature vectors and the further processing of the image only requires us to deal with the feature vectors rather than the image itself. This saves us a lot of processing time and is very easy to handle.

3.2 Organisation of chapter

The rest of the chapter is organized as follows: The system model for classifying retinal fundus images will be discussed in Section 3.3. Section 3.4 provides the detailed explanation of the LWP technique for generating the feature vectors.

3.3 System model

Figure 3.1 depicts the block diagram for the proposed framework. The input database images, the LWP feature extraction technique, data pre-processing, and classifier are some of the major blocks of the automated system model.

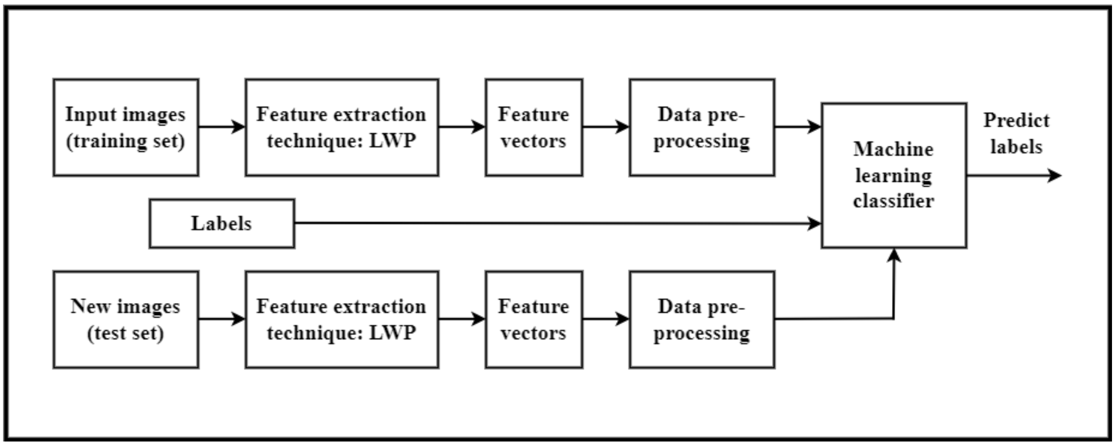

Figure 3.1: System model

The input database images (fundus images) are fed to the LWP image descriptor. We will use images from two publicly available databases for our project. For each image it generates a unique feature vector characterizing the image with a minimum set of real numbers. This feature vector then goes through the data pre-processing unit in order to make it suitable for the classifier. We have used the waikato environment for knowledge analysis (WEKA) tool in order to pre-process the feature vectors by applying relevant filters. The above mentioned process is applied to all the images in the databases. Then the labels or ground truth are appended to the pre-processed feature vectors in order to obtain the resultant feature matrix.

We have used the Classification Learner app of MATLAB to classify the feature vectors [51]. The Classification Learner app of MATLAB consists of 24 different classifiers such as support vector machine (SVM) [52], K nearest neighbors [53], bagged tree [54], logistic regression [55], linear discrimininant [56], etc. then train the machine learning (ML) model with this training data and appropriately calculates the weights. Whenever the trained ML model encounters the pre-processed feature vector of a new fundus image (a test image), it predicts the class or label of the image (0 for normal eye; 1 for glaucomatous eye).

3.4 The LWP image descriptor

The most important step in the system model is the LWP image descriptor which is responsible for characterizing the fundus image by a tuple of real numbers i.e. the feature vector. It retains the most important details of the image into the feature vector which is very easy to work with and significantly reduces the computational complexity of the further stages involved. Figure 3.2 depicts the keys steps involved in this technique.

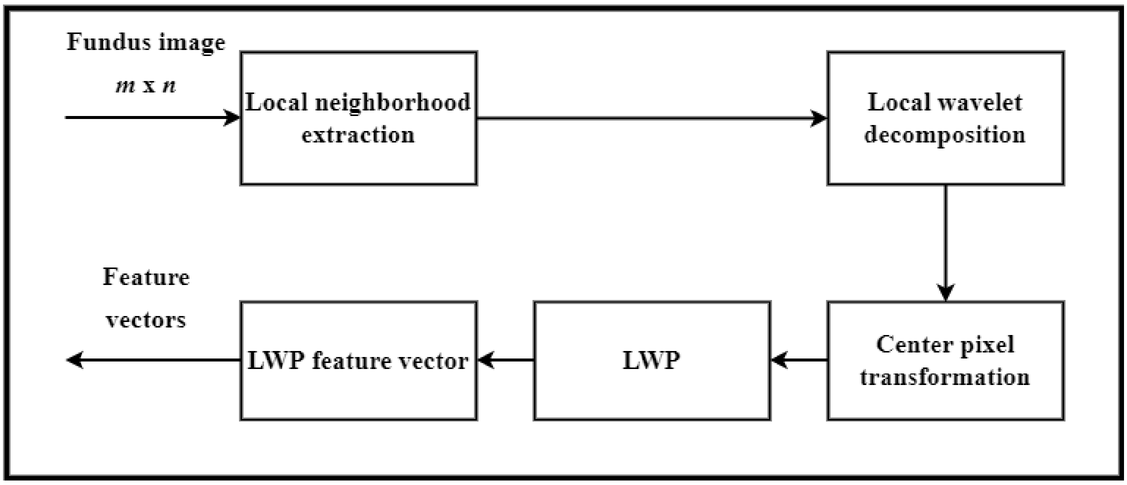

Figure 3.2: Key steps in LWP image descriptor

The five main elements or units of the LWP image descriptor are as follows:

1. Local neighborhood extraction
2. Local wavelet decomposition
3. Center pixel transformation
4. Local wavelet pattern generation
5. Feature vector generation

Consider a grayscale retinal fundus image F of dimension m x n as shown in Figure 3.3 below. This image will be used as the reference image for the entire chapter.

Figure 3.3: Reference fundus image

Every pixel of this image F at location (i,j) is denoted by $P^{i,j}$ and has an intensity I denoted by $I^{i,j}$. Note that we have padded the image so that we can consider the boundary pixels as well in the feature vector extraction process. In this section, we will first discuss the extraction of local neighbors for any given center pixel $P^{i,j}$. Then we will describe the local wavelet decomposition process for these extracted neighboring pixels. This will be followed by center pixel transformation operation. This step is followed by the construction of the local wavelet pattern for each pixel of the image. Finally we will generate the feature vector for the entire image.

3.4.1 Local neighborhood extraction

The local neighborhood extraction process is carried out for each and every pixel in the fundus image. It is the first step in the local wavelet pattern image descriptor process. The local neighbors with respect to a center pixel are derived in such a way that all of them are at the same radial distance from the center pixel. This property of the LWP is known as being radially symmetric. As already mentioned every pixel of the grayscale fundus image F of dimension m x n at location (i,j) is denoted by $P^{i,j}$ and has an intensity I denoted by $I^{i,j}$. Figure 3.4 shows the Cartesian coordinate system for the image with the origin at the upper left corner.

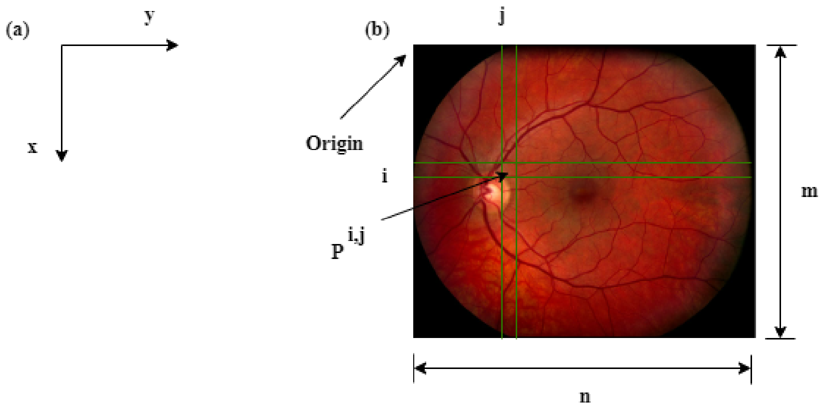

Figure 3.4: (a) Cartesian coordinate system and (b) the origin at the upper left corner and $P^{i,j}$ is the image pixel at location (i,j)

The K local neighbors of the center pixel $P^{i,j}$ are denoted as $L^{i,j}_{R,K}$. These local neighbors are symmetrically distributed at a circle of radius R having $P^{i,j}$ as its center. We denote the t^{th} neighbor of $P^{i,j}$ i.e. the t^{th} element of the vector $L^{i,j}_{R,K}$ as $L^{i,j}_{R,K,t}$. This element has the corresponding intensity value denoted as $I^{i,j}_{R,K,t}$, where $t \in [1,K]$ and it is a positive integer.

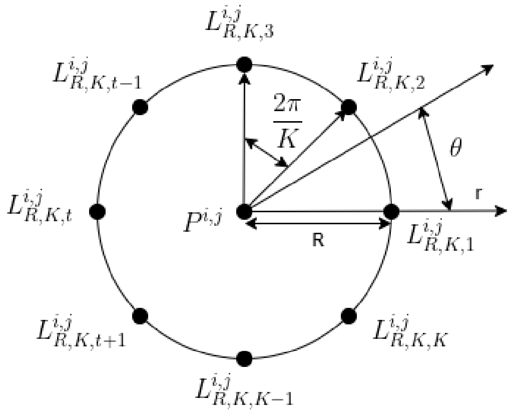

Figure 3.5: The polar coordinate system showing the K local neighbors $L^{i,j}_{R,K}$ with respect to a center pixel $P^{i,j}$

The coordinate of $L^{i,j}_{R,K,t}$ with respect to $P^{i,j}$ in the Cartesian coordinate system is given as follows:

$$x(L^{i,j}_{R,K,t}) = i - r(L^{i,j}_{R,K,t})\sin(\theta(L^{i,j}_{R,K,t})) \tag{3.1}$$

$$y(L^{i,j}_{R,K,t}) = j + r(L^{i,j}_{R,K,t})\cos(\theta(L^{i,j}_{R,K,t})) \tag{3.2}$$

where $i \in [R+1, m-R]$ and $j \in [R+1, n-R]$. Also note that $r(L^{i,j}_{R,N,t})$ and $\theta(L^{i,j}_{R,N,t})$ are the coordinates of $L^{i,j}_{R,N,t}$ in the Polar coordinate system with respect to the center pixel $P^{i,j}$ and is described by the equations given below.

$$r(L^{i,j}_{R,N,t}) = R \tag{3.3}$$

$$\theta(L^{i,j}_{R,N,t}) = (t-1)\frac{2\pi}{K} \tag{3.4}$$

3.4.2 Local wavelet decomposition

Having examined the procedure of determining the K local neighbors of a center pixel in the previous section, let us now see how we use the wavelet transform to decompose the neighboring pixels in order to establish a relationship among them. Let $I^{i,j}_{R,K,t}$ denotes the intensity value of the $t^{\mathbf{th}}$ neighbor of the center pixel, $\forall t \in [1,K]$. The intensity value of these K neighbors is used to derive the relationship that exists among them using one-dimensional Haar wavelet transform. This transform converts the intensity value $I^{i,j}_{R,K,t}$ into $Z^{i,j,d}_{R,K,t}$, $\forall t \in [1,K]$. Note that d is the level of decomposition or transformation. In other words the vector of intensity values I is converted into another vector Z as a result of this transformation.

One important thing to keep in mind is that the K local neighbors of a center pixel and the level of decomposition d are coupled to each other. Their dependence is captured by the following equation:

$$rem(K, 2^d) = 0 \tag{3.5}$$

where $rem(p,q)$ is the remainder function and it calculates the remainder obtained when q divides p. Also note that the maximum level of decomposition d, denoted by $d_{\max}$ is related to the number of local neighbors K by the following mathematical inequality:

$$2^{d_{\max}-1} \leq K \leq 2^{d_{\max}} \tag{3.6}$$

We have used the MATLAB function *wavedec* in order to perform the one-dimensional Haar wavelet transform of the K-tuple of intensity values of the local neighbors of the center pixel. The usage of the MATLAB function is as follows:

$$[Z,b] = wavedec(I,d,wav) \tag{3.7}$$

The *wavedec* function returns the wavelet decomposition of the one-dimensional vector of intensity values I in the output vector Z, at level d with the help of the wavelet *wav*. We parse the wavelet decomposed vector Z using the bookkeeping vector b. Figure 3.6 shows 8 local wavelet decomposed images for our reference fundus image in Figure 3.3. These 8 images are obtained for the parameter values of R = 3, K = 8, d = 3 and correspond to t = 1,2,...,8.

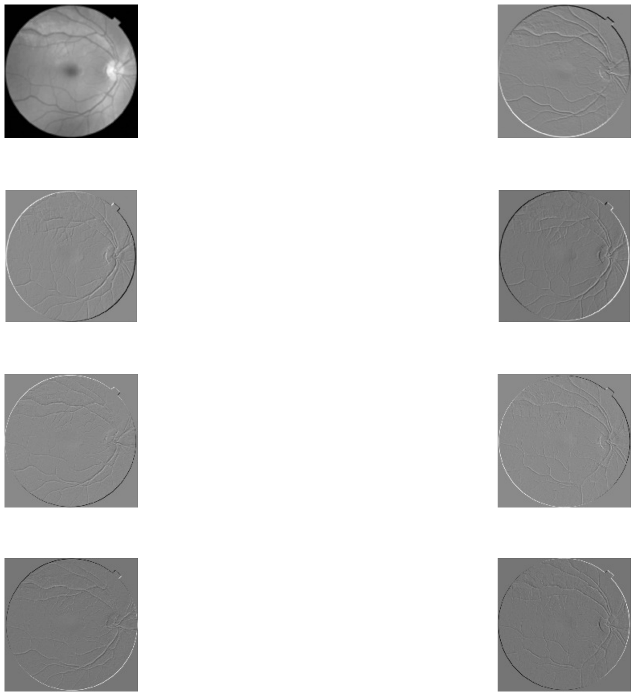

Figure 3.6: The 8 local wavelet decomposed images for the parameter values $R = 3$, $K = 8$, $d = 3$

These 8 images are obtained after performing local wavelet decomposition and contain a lot of information which is useful in the further stages of feature vector generation.

3.4.3 Center pixel transformation

In the previous section we used local wavelet decomposition (1-D Haar wavelet transform) in order to establish the relationship among $P^{i,j}_{R,K}$ (the K local neighbors) of the center pixel $P^{i,j}$. However, we have to eventually establish the relationship between $P^{i,j}_{R,K,t}$ and $P^{i,j}$. In the literature survey we have seen that most of the local methods directly use the intensity values ($I^{i,j}_{R,K}$) of the neighboring pixels. But with the LWP technique we will use the wavelet decomposed values of the neighboring pixels at level d or in other words $H^{i,j,d}_{R,K}$ in order to compare with the intensity value of the center pixel $I^{i,j}$. There is an inherent issue with this comparison because $H^{i,j,d}_{R,K}$ now occupies a different range of values as opposed to $I^{i,j}$ because of the wavelet decomposition. In order to circumvent this issue, we introduce the concept of transforming the center pixel intensity value. This technique converts $I^{i,j}$ into an array of size K at level d denoted by $T^{i,j,d}_{K,t}$, $\forall t \in [1,K]$. The recursive equation that governs the above transformation is defined as follows:

$$T^{i,j,d}_{K,t} = \begin{cases} 2^{(\frac{d}{2})} * I^{i,j} & \text{if } 1 \leq t \leq \frac{K}{2^d} \\ 2^{(\frac{d}{2})} * I^{i,j} - 2^{(\frac{d}{2})-1} * (l-1) & \text{if } \frac{K}{2^d} < t \leq \frac{K}{2^{d-1}} \\ T^{i,j,d-1}_{K,t} & \text{otherwise} \end{cases} \tag{3.8}$$

where l represents the number of gray levels the image F possesses.

After having performed the transformation of the center pixel it is now a vector whose values are in a similar range as that of the wavelet decomposed neighbors $H^{i,j,d}_{R,K}$ for all the K neighbors. Figure 3.7 shows 8 center pixel transformed images for our reference fundus image in Figure 3.3. These 8 images are obtained for the parameter values of R = 3, K = 8, d = 3 and correspond to t = 1,2,...,8.

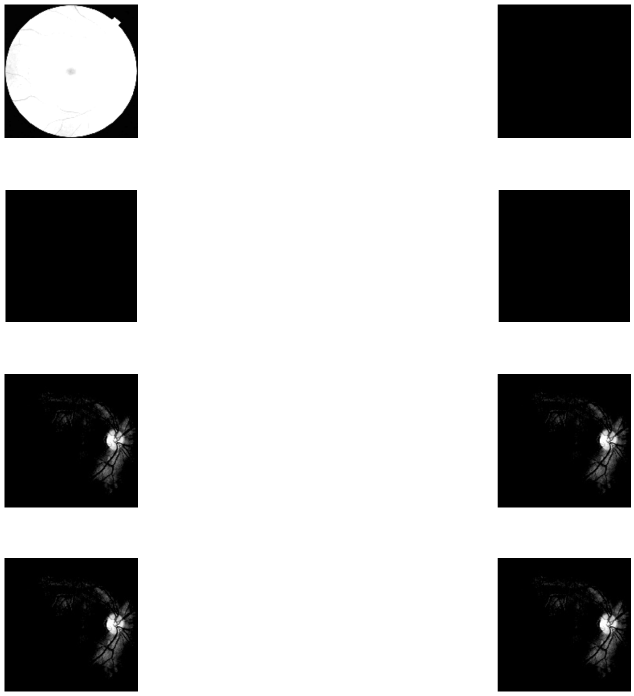

Figure 3.7: The 8 center pixel transformed images for the parameter values R = 3, K = 8, d = 3

Although it is not clearly obvious, but these images have varying intensity ranges and are now having similar values as that of the intensity vector of 8 local neighbors.

3.4.4 LWP generation

In the previous sections we have derived the vector of K wavelet decomposed neighbors at level d denoted by $H^{i,j,d}_{R,K}$ and the vector of K values for the center pixel at level d obtained by the center pixel transformation technique and denoted by $T^{i,j,d}_{K,t}$. Now the two vectors are having similar range of values and are amenable for comparison. In this section we will derive the relationship between the center pixel and its K neighbors (i.e. between $P^{i,j}$ and $P^{i,j}_{R,K}$) with the help of these two vectors by encoding them in binary format (having 0's and 1's). This form of encoding is termed as LWP. It is a vector of K values where each value corresponds to a neighbor of the center pixel $P^{i,j}$. The equations involved in the encoding process are explained below:

$$Q^{i,j,d}_{R,K} = \left[Q^{i,j,d}_{R,K,1} Q^{i,j,d}_{R,K,2} \ldots Q^{i,j,d}_{R,K,K} \right] \tag{3.9}$$

where $Q^{i,j,d}_{R,N,t}$ represents a local wavelet pattern binary value for the t^{th} neighbor of the center pixel $P^{i,j}$ and is obtained in the following manner:

$$Q^{i,j,d}_{R,K,t} = f(diff^{i,j,d}_{R,K,t}) \tag{3.10}$$

where $diff$ is a difference function and is defined as follows:

$$diff(a) = \begin{cases} 1 & \text{if } a > 0 \\ 0 & \text{otherwise} \end{cases} \tag{3.11}$$

and $diff^{i,j,d}_{R,K,t}$ is the t^{th} element of the difference vector (i.e. difference between the vectors $H^{i,j,d}_{R,K}$ and $T^{i,j,d}_{K,t}$ at the same level d) for the center pixel $P^{i,j}$ and is mathematically defined in the following manner:

$$diff^{i,j,d}_{R,K,t} = H^{i,j,d}_{R,K,t} - T^{i,j,d}_{K,t} \tag{3.12}$$

Also the map of the LWPs denoted by $Qm^{i,j,d}_{R,K}$ for the center pixel $P^{i,j}$ is obtained by using the vector $Q^{i,j,d}_{R,K}$ using the equation mentioned below:

$$Qm^{i,j,d}_{R,K} = \sum_{t=1}^{K} 2^{t-1} * Q^{i,j,d}_{R,K,t} \tag{3.13}$$

The pattern map $Qm^{i,j,d}_{R,K}$ for the center pixel $P^{i,j}$ is dependent on the number of neighbors of the center pixel (i.e. K) and its resultant value lies in the range 0 to $2^K - 1$.

Figure 3.8 shows 8 LWPs for our reference fundus image in Figure 3.3. These 8 images are obtained for the parameter values of $R = 3$, $K = 8$, $d = 3$ and correspond to $t = 1,2,...,8$. We have used the 8 local wavelet decomposed images in Figure 3.6 and the 8 center pixel transformed images in Figure 3.7 in order to form these 8 images.

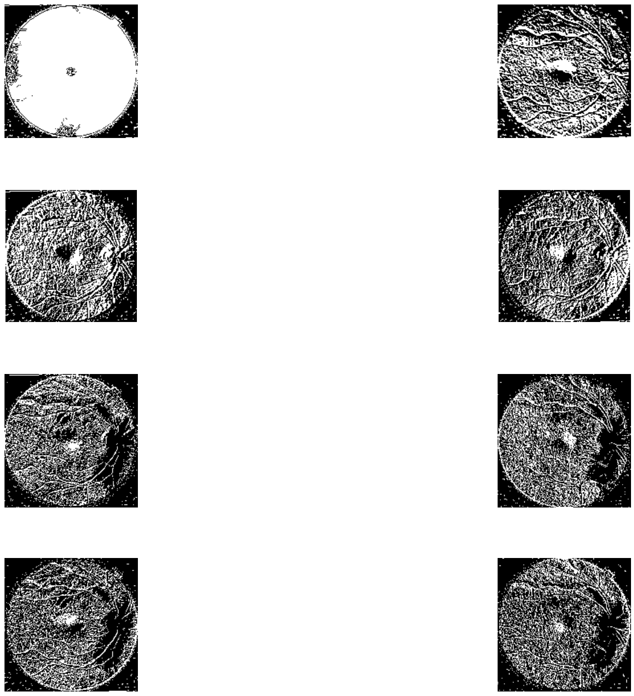

Figure 3.8: The 8 LWPs for the parameter values $R = 3$, $K = 8$, $d = 3$

Finally we have also depicted the LWP map for our reference fundus image (Figure 3.3) in Figure 3.9.

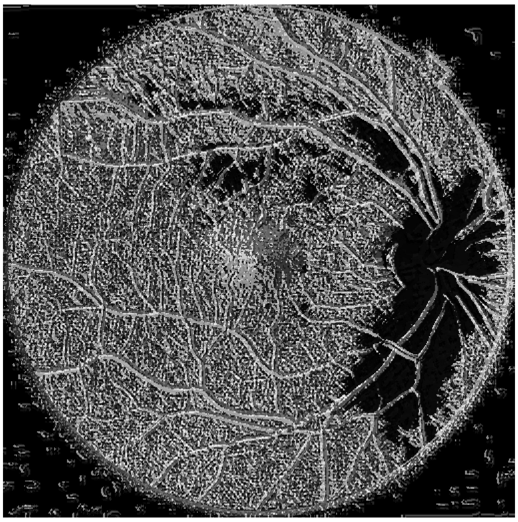

Figure 3.9: The LWP map for the parameter values R = 3, K = 8, d = 3

Note that the LWP map of the reference fundus image has a lot of detailed information and plays a crucial role in the generation of feature vectors.

3.4.5 Feature vector generation

In the previous section we derived the local wavelet pattern vector $Q^{i,j,d}_{R,N,t}$ which was a binary array (consisting of only 0's and 1's) and also the pattern map using this vector denoted by $Qm^{i,j,d}_{R,K}$. In this section we will finally derive the LWP feature vector for the entire fundus image.

In order to obtain the feature vector FV for the entire fundus image F, we consider the LWP map Qm of each and every pixel P of the image. It is denoted by $FV^{d}_{R,K}(\varepsilon)$, where d is the level of wavelet decomposition, R is the radius considered to obtain the K local neighbors; and is derived using the following mathematical equation:

$$FV^{d}_{R,K}(\varepsilon) = \frac{1}{\widehat{\omega 1} * \widehat{\omega 2}} \sum_{i=R+1}^{m-R} \sum_{j=R+1}^{n-R} C(Qm^{i,j,d}_{R,K}, \varepsilon) \tag{3.14}$$

where m and n are the dimensions of the fundus image F, ε is an integer between 0 and $2^K - 1$ (i.e. $\varepsilon \in [0, 2^K - 1]$). Also note that $\widehat{\omega 1} = m - 2R$ and $\widehat{\omega 2} = n - 2R$. The function $C(a,b)$ is expressed as follows:

$$C(a,b) = \begin{cases} 1 & \text{if } a = b \\ 0 & \text{otherwise} \end{cases} \tag{3.15}$$

The resulting feature vectors for the corresponding retinal fundus images can be used along with the ground truths/labels to form the feature matrix. This matrix is finally fed to the machine learning classifier in order to train the model (i.e. obtain the appropriate weights) for our binary classification problem.

Chapter 4

Simulation, Results, and Discussion

4.1 Introduction

We have seen the system model for our proposed method and the local wavelet pattern (LWP) image descriptor in some detail in the previous section. In this section we will present the simulations that were carried out on two publicly available databases for retinal fundus images and the corresponding results. We will also note some of the effects the parameters of the LWP descriptor has on the overall binary classification of retinal fundus images.

4.2 Organization of chapter

The chapter is organized in the following manner: First the simulation and results will be discussed for the first database (i.e. r1 database) in Section 4.2. Then we will present the simulation and results for the second database (i.e. r2 database) in section Section 4.3. Finally we present the results obtained for local binary pattern (LBP) and local ternary pattern (LTP) in Section 4.4 and compare these results with our proposed method (i.e. LWP).

4.3 Results for r1 database

We have carried out the simulation for 30 different combinations for our three parameters namely the radius of local neighborhood (R), the number of local neighbors (K) and the level of wavelet decomposition (d). The results have been summarized in the following two tables for the r1 database.

Table 4.1: Simulation results for database 1 - RIM-ONE r1 before data pre-processing

Sr. No.	Parameter Values	Classifier	Accuracy
1	$R = 1, K = 2, d = 1$	Logistic regression & SVM (Quadratic SVM)	71.6%
2	$R = 2, K = 2, d = 1$	Logistic regression & SVM (Quadratic SVM)	74.0%
3	$R = 3, K = 2, d = 1$	Linear discriminant	73.4%
4	$R = 4, K = 2, d = 1$	SVM (Quadratic SVM)	74.0%
5	$R = 1, K = 4, d = 1$	Linear discriminant	82.2%
6	$R = 2, K = 4, d = 1$	Logistic regression	78.7%
7	$R = 3, K = 4, d = 1$	SVM (Linear SVM)	79.3%
8	$R = 4, K = 4, d = 1$	Ensemble (Subspace discriminant)	79.9%
9	$R = 1, K = 6, d = 1$	SVM (Linear SVM) & Ensemble (Bagged trees)	75.7%
10	$R = 2, K = 6, d = 1$	SVM (Linear SVM)	81.1%
11	$R = 3, K = 6, d = 1$	SVM (Medium Gaussian SVM) & Ensemble (Bagged trees)	77.5%
12	$R = 4, K = 6, d = 1$	SVM (Medium Gaussian SVM)	79.3%
13	$R = 1, K = 8, d = 1$	SVM (Linear SVM)	79.9%
14	$R = 2, K = 8, d = 1$	SVM (Quadratic SVM)	78.7%
15	$R = 3, K = 8, d = 1$	SVM (Medium Gaussian SVM) & KNN (Fine KNN)	78.1%
16	$R = 4, K = 8, d = 1$	SVM (Quadratic SVM)	81.1%
17	$R = 1, K = 4, d = 2$	SVM (Linear SVM) & Ensemble (Bagged trees)	78.7%
18	$R = 2, K = 4, d = 2$	SVM (Medium Gaussian SVM)	80.5%
19	$R = 3, K = 4, d = 2$	Ensemble (Bagged trees)	81.1%
20	$R = 4, K = 4, d = 2$	SVM (Linear SVM)	78.1%

21	$R = 1, K = 8, d = 2$	SVM (Linear SVM) & SVM (Medium Gaussian SVM)	76.9%
22	$R = 2, K = 8, d = 2$	SVM (Linear SVM)	79.9%
23	$R = 3, K = 8, d = 2$	SVM (Medium Gaussian SVM)	80.5%
24	$R = 4, K = 8, d = 2$	SVM (Quadratic SVM)	82.2%
25	$R = 1, K = 8, d = 3$	SVM (Cubic SVM)	78.1%
26	$R = 2, K = 8, d = 3$	SVM (Quadratic SVM)	79.9%
27	$R = 3, K = 8, d = 3$	SVM (Quadratic SVM) & SVM (Cubic SVM)	76.9%
28	$R = 4, K = 8, d = 3$	SVM (Quadratic SVM)	79.9%
29	$R = 6, K = 8, d = 3$	SVM (Linear SVM)	79.9%
30	$R = 8, K = 8, d = 3$	SVM (Cubic SVM)	78.7%

As seen from Table 4.1, the best results are obtained for the following two cases:-

1. An accuracy of 82.2% is obtained for $R = 1$, $K = 4$, $d = 1$ for the linear discriminant classifier. The confusion matrix and the receiver operating characteristic (ROC) curve are shown in Figures. 4.1 and 4.2.

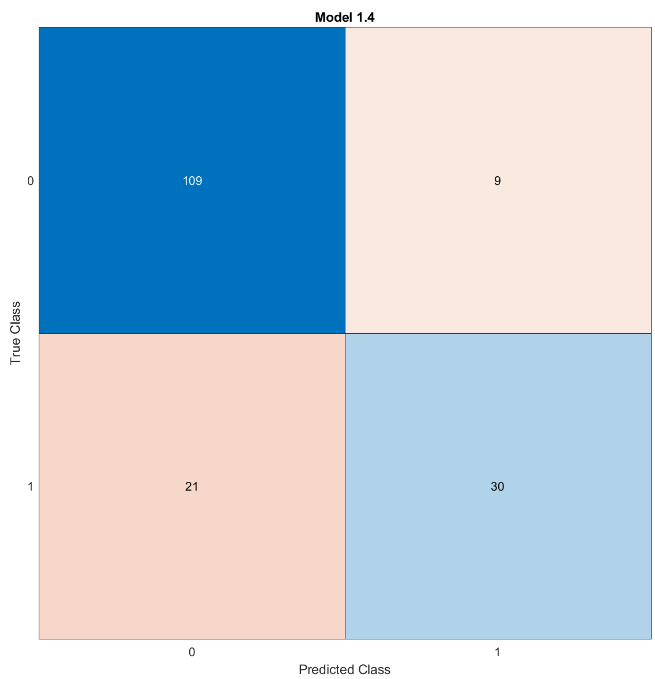

Figure 4.1: Confusion matrix for $R = 1$, $K = 4$, $d = 1$ for database 1 - RIM-ONE r1 before data pre-processing

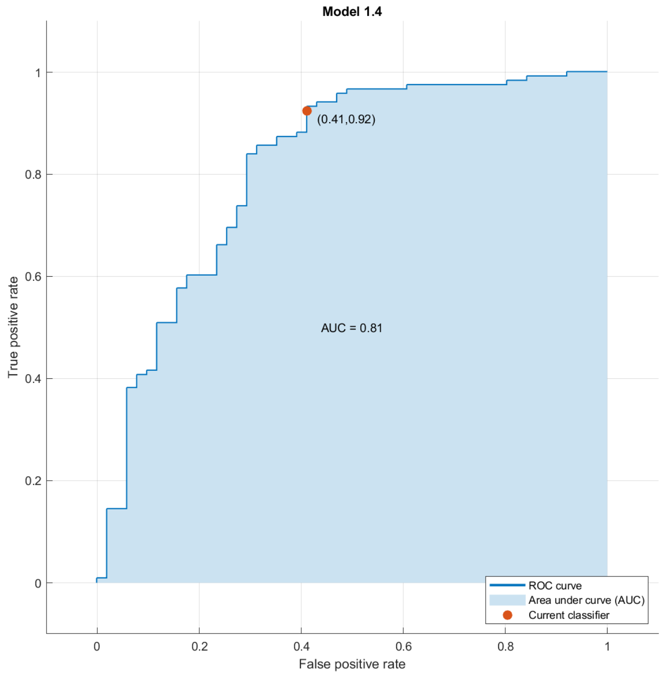

Figure 4.2: Receiver operating characteristic (ROC) for $R = 1$, $K = 4$, $d = 1$ for database 1 - RIM-ONE r1 before data pre-processing

2. An accuracy of 82.2% is obtained for $R = 4$, $K = 8$, $d = 2$ for the SVM classifier. The confusion matrix and the receiver operating characteristic (ROC) curve are shown in Figures. 4.3 and 4.4.

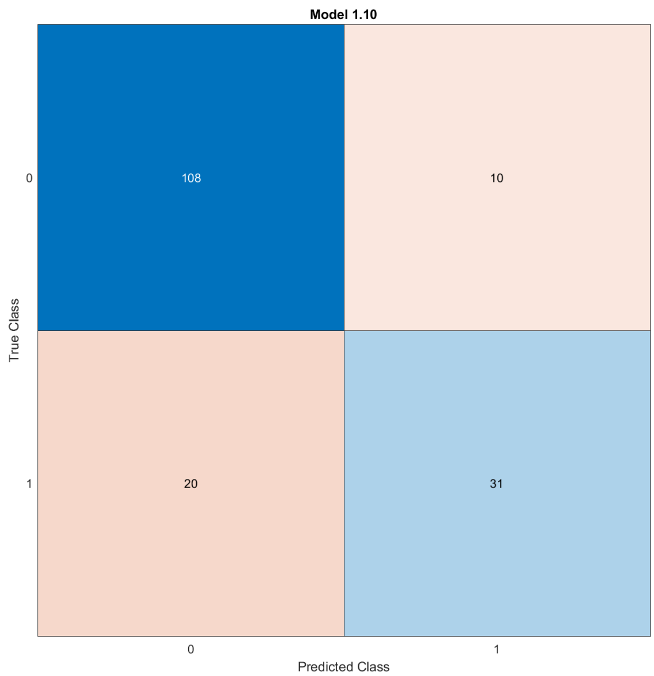

Figure 4.3: Confusion matrix for $R = 4$, $K = 8$, $d = 2$ for database 1 - RIM-ONE r1 before data pre-processing

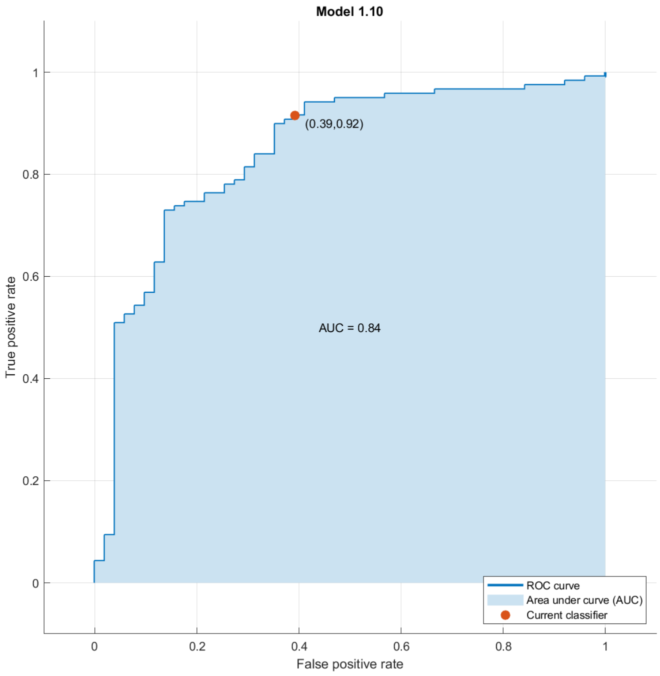

Figure 4.4: Receiver operating characteristic (ROC) for $R = 4$, $K = 8$, $d = 2$ for database 1 - RIM-ONE r1 before data pre-processing

Table 4.2: Simulation results for database 1 - RIM-ONE r1 after data pre-processing

Sr. No.	Parameter Values	Classifier	Accuracy
1	$R = 1, K = 2, d = 1$	KNN (Weighted KNN)	90.5%
2	$R = 2, K = 2, d = 1$	KNN (Weighted KNN)	91.7%
3	$R = 3, K = 2, d = 1$	KNN (Weighted KNN)	92.9%
4	$R = 4, K = 2, d = 1$	KNN (Fine KNN)	94.1%
5	$R = 1, K = 4, d = 1$	SVM (Cubic SVM)	92.3%
6	$R = 2, K = 4, d = 1$	SVM (Cubic SVM)	94.7%
7	$R = 3, K = 4, d = 1$	Logistic regression	97.0%
8	$R = 4, K = 4, d = 1$	Ensemble (RUSBoosted trees)	96.4%
9	$R = 1, K = 6, d = 1$	SVM (Cubic SVM)	94.7%
10	$R = 2, K = 6, d = 1$	SVM (Quadratic SVM) & SVM (Cubic SVM)	91.7%
11	$R = 3, K = 6, d = 1$	Logistic Regression	96.4%
12	$R = 4, K = 6, d = 1$	Ensemble (Bagged trees)	95.9%
13	$R = 1, K = 8, d = 1$	SVM (Quadratic SVM)	96.4%
14	$R = 2, K= 8, d = 1$	SVM (Quadratic SVM)	97.0%
15	$R = 3, K = 8, d = 1$	Linear Discriminant & SVM (Quadratic SVM) & SVM (Cubic SVM)	94.1%
16	$R = 4, K = 8, d = 1$	SVM (Quadratic SVM) & SVM (Cubic SVM)	96.4%
17	$R = 1, K = 4, d = 2$	SVM (Cubic SVM)	94.7%
18	$R = 2, K = 4, d = 2$	SVM (Cubic SVM)	96.4%
19	$R = 3, K = 4, d = 2$	KNN (Fine KNN)	94.1%
20	$R = 4, K = 4, d = 2$	Ensemble (RUSBoosted trees)	92.3%

21	$R = 1, K = 8, d = 2$	Linear discriminant & SVM (Quadratic SVM) & Ensemble (Subspace discriminant)	93.5%
22	$R = 2, K = 8, d = 2$	SVM (Quadratic SVM)	95.9%
23	$R = 3, K = 8, d = 2$	SVM (Quadratic SVM)	95.9%
24	$R = 4, K = 8, d = 2$	SVM (Quadratic SVM) & SVM (Cubic SVM) & KNN (Fine KNN) & Ensemble (Subspace discriminant)	95.3%
25	$R = 1, K = 8, d = 3$	SVM (Quadratic SVM)	94.1%
26	$R = 2, K = 8, d = 3$	SVM (Quadratic SVM)	94.7%
27	$R = 3, K = 8, d = 3$	SVM (Quadratic SVM)	97.0%
28	$R = 4, K = 8, d = 3$	Ensemble (RUSBoosted trees)	95.9%
29	$R = 6, K = 8, d = 3$	Linear discriminant	94.7%
30	$R = 8, K = 8, d = 3$	SVM (Quadratic SVM)	96.4%

As seen from Table 4.2, the best results are obtained for the following three cases:-

1. An accuracy of 97.0% is obtained for $R = 3$, $K = 4$, $d = 1$ for the Logistic Regression classifier. The confusion matrix and the receiver operating characteristic (ROC) curve are shown in Figures. 4.5 and 4.6.

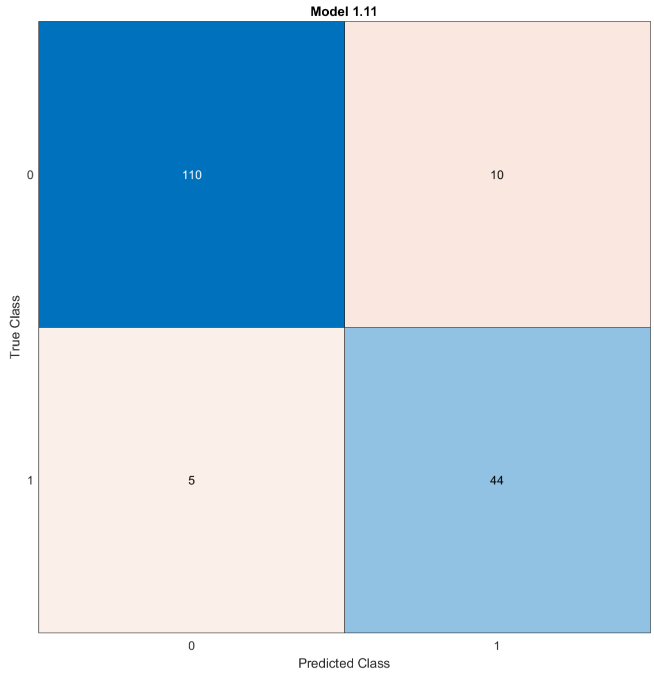

Figure 4.5: Confusion matrix for $R = 3$, $K = 4$, $d = 1$ for database 1 - RIM-ONE r1 after data pre-processing

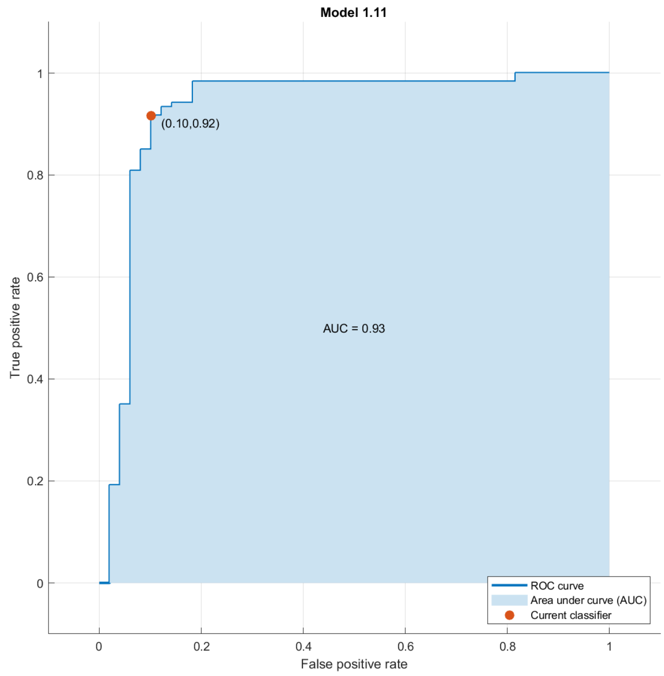

Figure 4.6: Receiver operating characteristic (ROC) for $R = 3$, $K = 4$, $d = 1$ for database 1 - RIM-ONE r1 after data pre-processing

2. An accuracy of 97.0% is obtained for $R = 2$, $K = 8$, $d = 1$ for the SVM classifier. The confusion matrix and the receiver operating characteristic (ROC) curve are shown in Figures. 4.7 and 4.8.

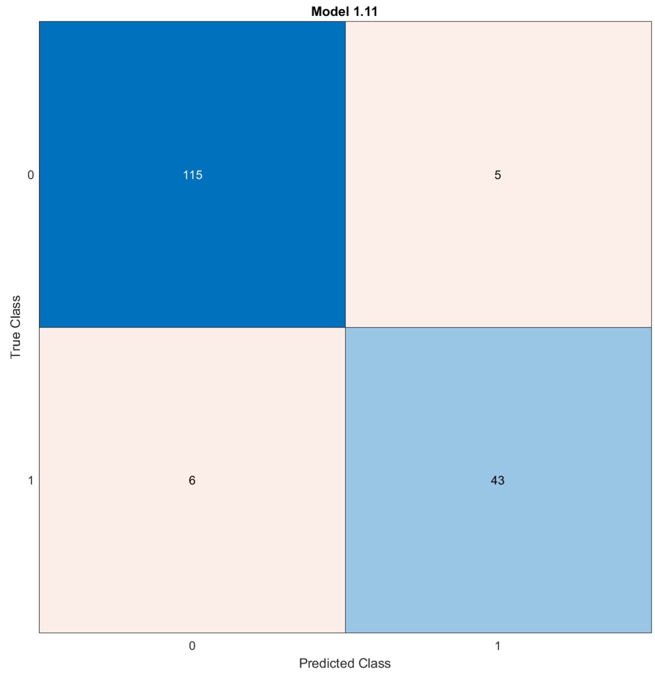

Figure 4.7: Confusion matrix for $R = 2$, $K = 8$, $d = 1$ for database 1 - RIM-ONE r1 after data pre-processing

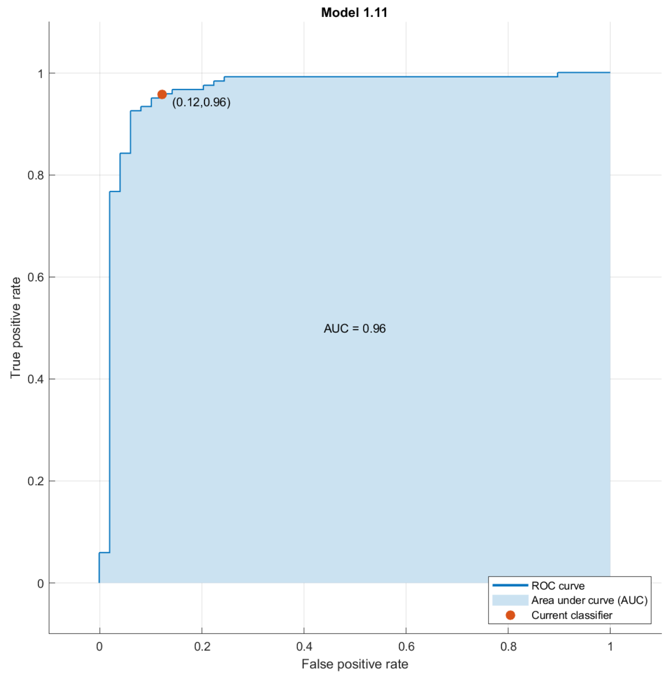

Figure 4.8: Receiver operating characteristic (ROC) for $R = 2$, $K = 8$, $d = 1$ for database 1 - RIM-ONE r1 after data pre-processing

3. An accuracy of 97.0% is obtained for $R = 3$, $K = 8$, $d = 3$ for the SVM classifier. The confusion matrix and the receiver operating characteristic (ROC) curve are shown in Figures. 4.9 and 4.10.

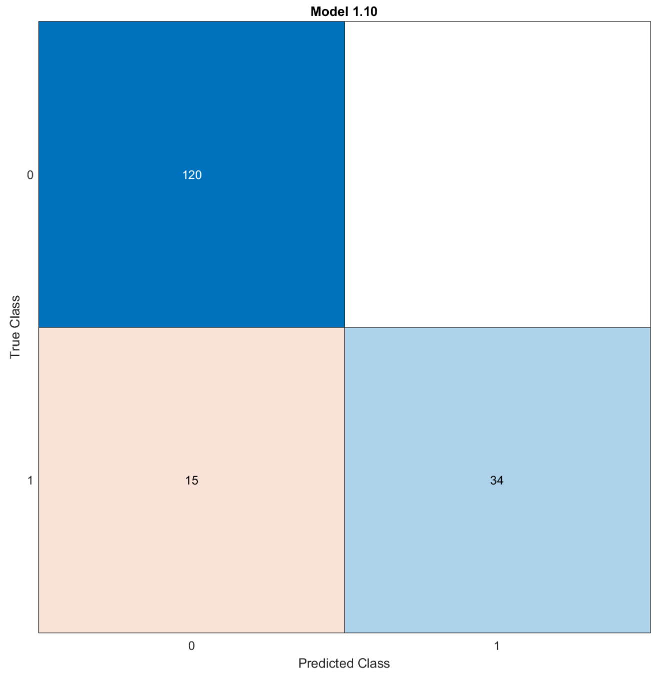

Figure 4.9: Confusion matrix for $R = 3$, $K = 8$, $d = 3$ for database 1 - RIM-ONE r1 after data pre-processing

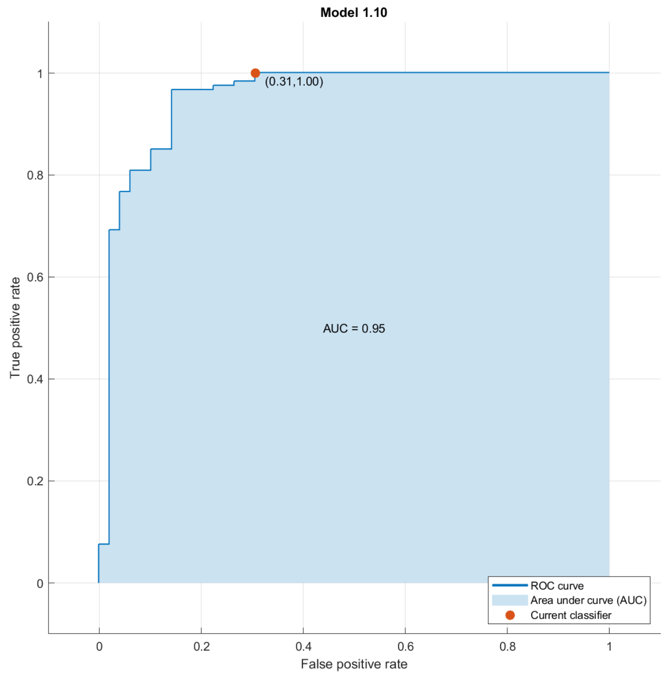

Figure 4.10: Receiver operating characteristic (ROC) for $R = 3$, $K = 8$, $d = 3$ for database 1 - RIM-ONE r1 after data pre-processing

4.4 Results for r2 Database

We have carried out the simulation for 30 different combinations for our three parameters namely the radius of local neighborhood (R), the number of local neighbors (K) and the level of wavelet decomposition (d). The results have been summarized in the following two tables for the r2 database.

Table 4.3: Simulation results for database 2 - RIM-ONE r2 before data pre-processing

Sr. No.	Parameter Values	Classifier	Accuracy
1	$R = 1, K = 2, d = 1$	SVM (Fine Gaussian SVM)	65.5%
2	$R = 2, K = 2, d = 1$	SVM (Linear SVM)	61.1%
3	$R = 3, K = 2, d = 1$	SVM (Quadratic SVM)	60.0%
4	$R = 4, K = 2, d = 1$	SVM (Fine Gaussian SVM)	62.2%
5	$R = 1, K = 4, d = 1$	SVM (Quadratic SVM)	82.4%
6	$R = 2, K = 4, d = 1$	Ensemble (Bagged trees)	80.7%
7	$R = 3, K = 4, d = 1$	SVM (Quadratic SVM)	81.8%
8	$R = 4, K = 4, d = 1$	SVM (Quadratic SVM)	80.7%
9	$R = 1, K = 6, d = 1$	SVM (Medium Gaussian SVM)	83.1%
10	$R = 2, K = 6, d = 1$	SVM (Medium Gaussian SVM)	82.2%
11	$R = 3, K = 6, d = 1$	SVM (Cubic SVM)	83.7%
12	$R = 4, K = 6, d = 1$	SVM (Cubic SVM)	84.6%
13	$R = 1, K = 8, d = 1$	SVM (Quadratic SVM)	85.5%
14	$R = 2, K = 8, d = 1$	SVM (Quadratic SVM)	86.4%
15	$R = 3, K = 8, d = 1$	SVM (Cubic SVM)	84.8%
16	$R = 4, K = 8, d = 1$	SVM (Cubic SVM)	85.7%
17	$R = 1, K = 4, d = 2$	SVM (Quadratic SVM)	84.0%
18	$R = 2, K = 4, d = 2$	SVM (Quadratic SVM)	83.5%
19	$R = 3, K = 4, d = 2$	SVM (Quadratic SVM)	82.2%
20	$R = 4, K = 4, d = 2$	SVM (Quadratic SVM)	81.5%

21	$R = 1, K = 8, d = 2$	SVM (Quadratic SVM)	85.3%
22	$R = 2, K = 8, d = 2$	SVM (Quadratic SVM)	86.4%
23	$R = 3, K = 8, d = 2$	SVM (Cubic SVM)	86.4%
24	$R = 4, K = 8, d = 2$	SVM (Cubic SVM)	84.0%
25	$R = 1, K = 8, d = 3$	SVM (Cubic SVM)	85.9%
26	$R = 2, K = 8, d = 3$	SVM (Medium Gaussian SVM)	86.2%
27	$R = 3, K = 8, d = 3$	SVM (Medium Gaussian SVM)	85.3%
28	$R = 4, K = 8, d = 3$	SVM (Cubic SVM)	84.2%
29	$R = 6, K = 8, d = 3$	SVM (Cubic SVM)	84.4%
30	$R = 8, K = 8, d = 3$	SVM (Cubic SVM)	80.7%

As seen from Table 4.3, the best results are obtained for the following three cases:-

1. An accuracy of 86.4% is obtained for $R = 2$, $K = 8$, $d = 1$ for the SVM classifier. The confusion matrix and the receiver operating characteristic (ROC) curve are shown in Figures. 4.11 and 4.12.

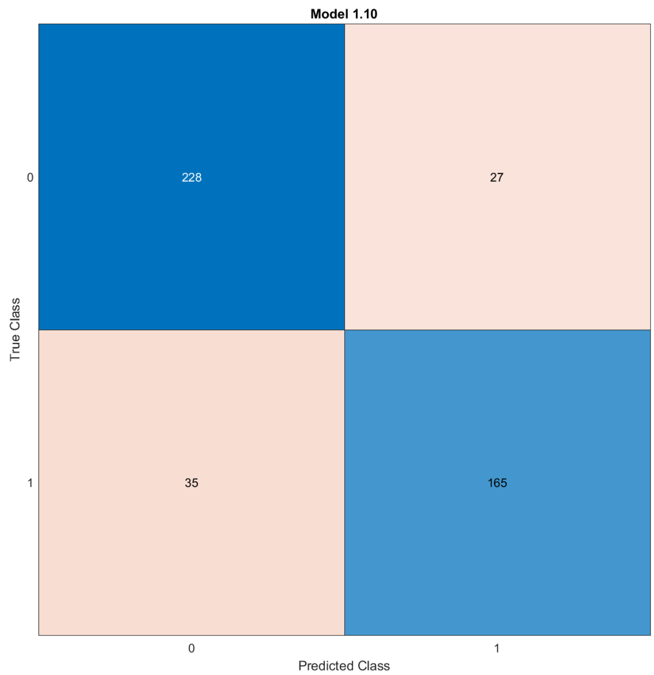

Figure 4.11: Confusion matrix for $R = 2$, $K = 8$, $d = 1$ for database 2 - RIM-ONE r2 before data pre-processing

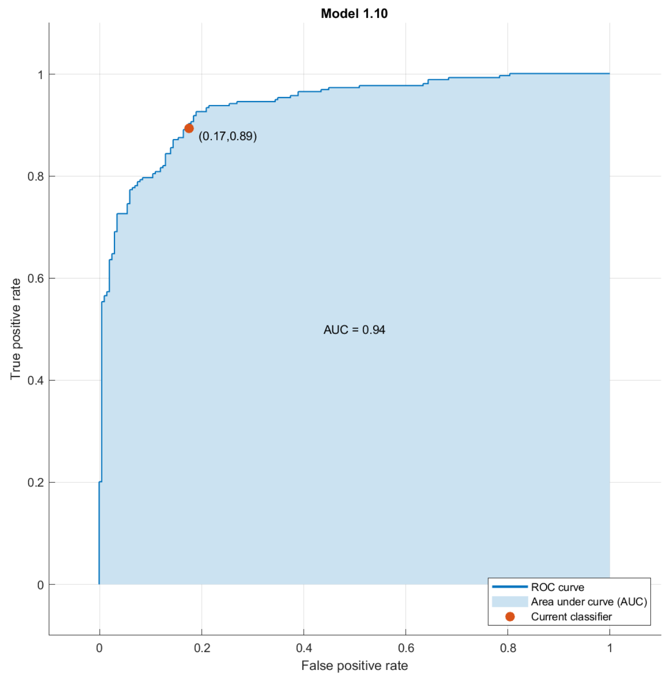

Figure 4.12: Receiver operating characteristic (ROC) for R = 2, K = 8, d = 1 for database 2 - RIM-ONE r2 before data pre-processing

2. An accuracy of 86.4% is obtained for R = 2, K = 8, d = 2 for the SVM classifier. The confusion matrix and the receiver operating characteristic (ROC) curve are shown in Figures. 4.13 and 4.14.

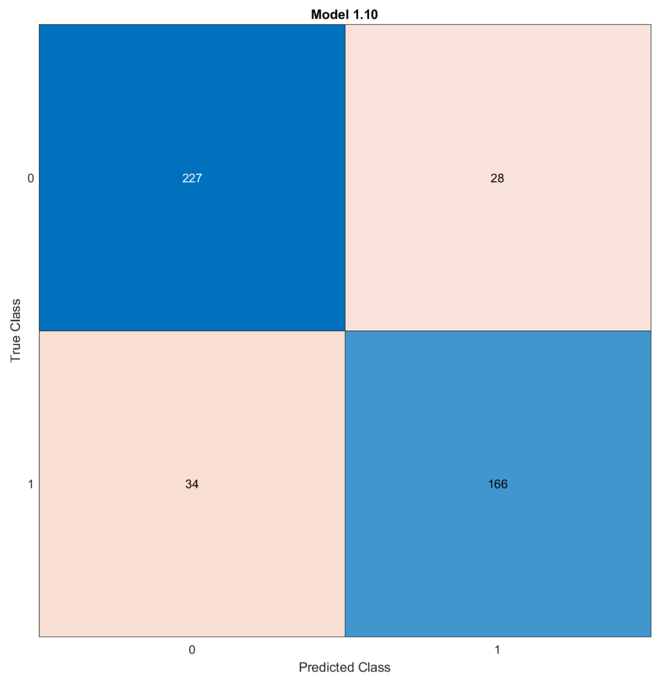

Figure 4.13: Confusion matrix for R = 2, K = 8, d = 2 for database 2 - RIM-ONE r2 before data pre-processing

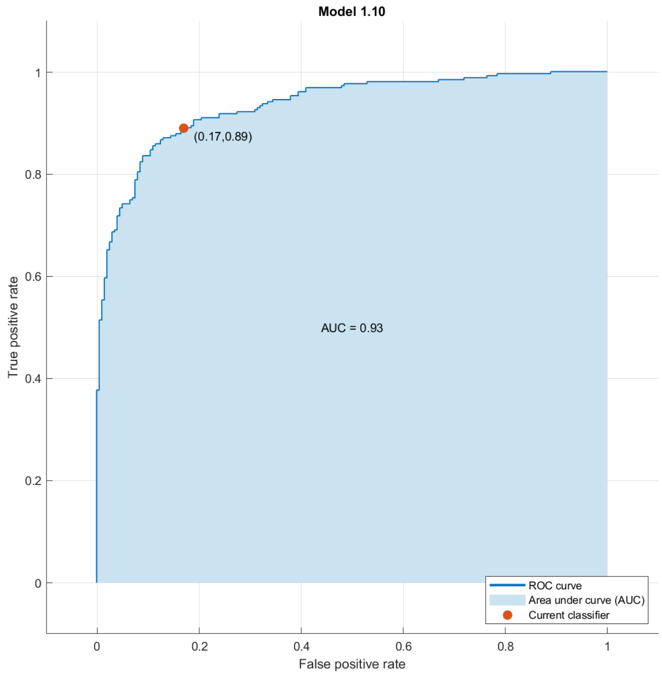

Figure 4.14: Receiver operating characteristic (ROC) for R = 2, K = 8, d = 2 for database 2 - RIM-ONE r2 before data pre-processing

3. An accuracy of 86.4% is obtained for R = 3, K = 8, d = 2 for the SVM classifier. The confusion matrix and the receiver operating characteristic (ROC) curve are shown in Figures. 4.15 and 4.16.

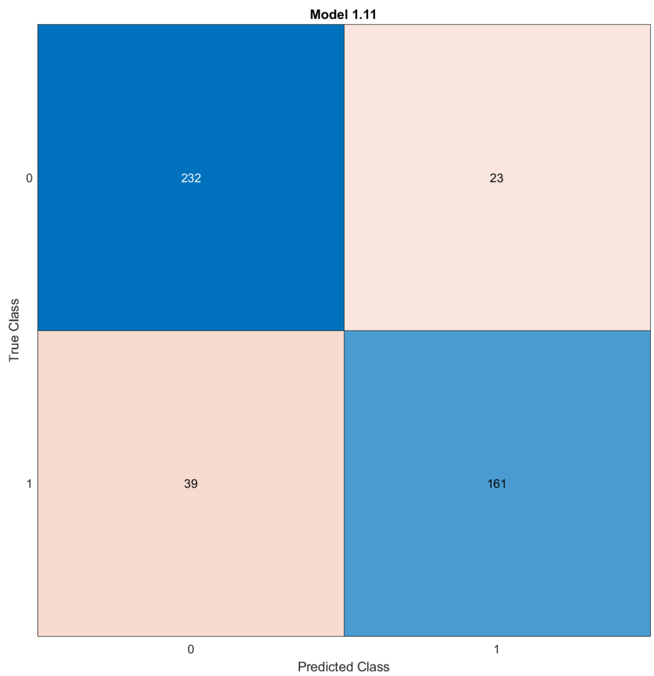

Figure 4.15: Confusion matrix for R = 3, K = 8, d = 2 for database 2 - RIM-ONE r2 before data pre-processing

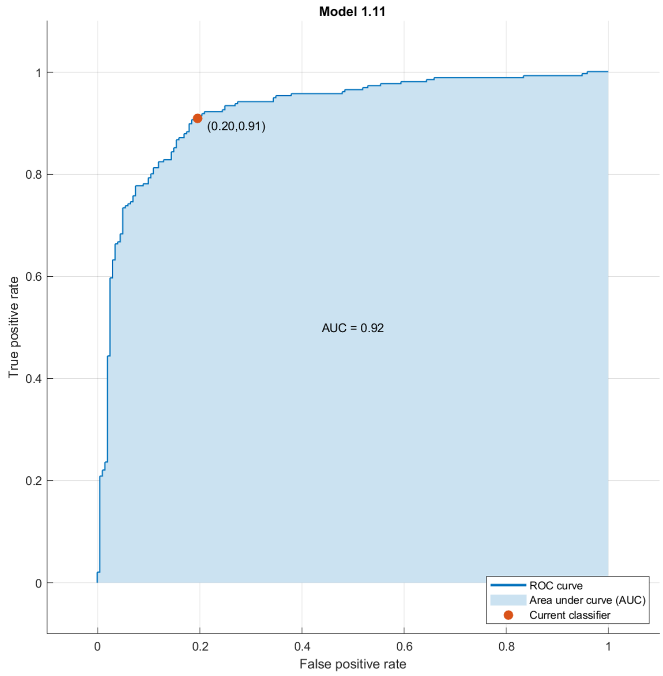

Figure 4.16: Receiver operating characteristic (ROC) for R = 3, K = 8, d = 2 for database 2 - RIM-ONE r2 before data pre-processing

Table 4.4: Simulation results for database 2 - RIM-ONE r2 after data pre-processing

Sr. No.	Parameter Values	Classifier	Accuracy
1	$R = 1, K = 2, d = 1$	Ensemble (Bagged trees)	84.0%
2	$R = 2, K = 2, d = 1$	Ensemble (Subspace KNN)	83.1%
3	$R = 3, K = 2, d = 1$	KNN (Weighted KNN)	80.4%
4	$R = 4, K = 2, d = 1$	KNN (Weighted KNN)	83.1%
5	$R = 1, K = 4, d = 1$	Ensemble (Boosted trees)	90.8%
6	$R = 2, K = 4, d = 1$	Ensemble (Bagged trees)	91.0%
7	$R = 3, K = 4, d = 1$	Ensemble (Bagged trees)	90.3%
8	$R = 4, K = 4, d = 1$	Ensemble (Bagged trees)	89.9%
9	$R = 1, K = 6, d = 1$	SVM (Quadratic SVM)	92.7%
10	$R = 2, K = 6, d = 1$	SVM (Cubic SVM)	91.0%
11	$R = 3, K = 6, d = 1$	SVM (Cubic SVM)	91.6%
12	$R = 4, K = 6, d = 1$	SVM (Cubic SVM)	89.9%
13	$R = 1, K = 8, d = 1$	SVM (Quadratic SVM)	92.5%
14	$R = 2, K = 8, d = 1$	SVM (Cubic SVM)	92.7%
15	$R = 3, K = 8, d = 1$	SVM (Quadratic SVM)	91.2%
16	$R = 4, K = 8, d = 1$	SVM (Quadratic SVM)	90.5%
17	$R = 1, K = 4, d = 2$	KNN (Weighted KNN)	91.4%
18	$R = 2, K = 4, d = 2$	KNN (Weighted KNN) & Ensemble (Bagged trees)	88.8%
19	$R = 3, K = 4, d = 2$	KNN (Fine KNN)	89.2%
20	$R = 4, K = 4, d = 2$	KNN (Fine KNN)	90.1%

21	$R = 1, K = 8, d = 2$	SVM (Quadratic SVM)	93.0%
22	$R = 2, K = 8, d = 2$	SVM (Quadratic SVM)	92.5%
23	$R = 3, K = 8, d = 2$	KNN (Fine KNN)	92.3%
24	$R = 4, K = 8, d = 2$	KNN (Fine KNN)	89.9%
25	$R = 1, K = 8, d = 3$	SVM (Quadratic SVM)	91.6%
26	$R = 2, K = 8, d = 3$	SVM (Quadratic SVM)	91.9%
27	$R = 3, K = 8, d = 3$	SVM (Quadratic SVM)	91.9%
28	$R = 4, K = 8, d = 3$	SVM (Quadratic SVM)	91.9%
29	$R = 6, K = 8, d = 3$	SVM (Cubic SVM)	91.9%
30	$R = 8, K = 8, d = 3$	KNN (Fine KNN)	89.5%

As seen from Table 4.4, the best result is obtained for the following:-

1. An accuracy of 93.0% is obtained for $R = 1$, $K = 8$, $d = 2$ for the SVM classifier. The confusion matrix and the receiver operating characteristic (ROC) curve are shown in Figures. 4.17 and 4.18.

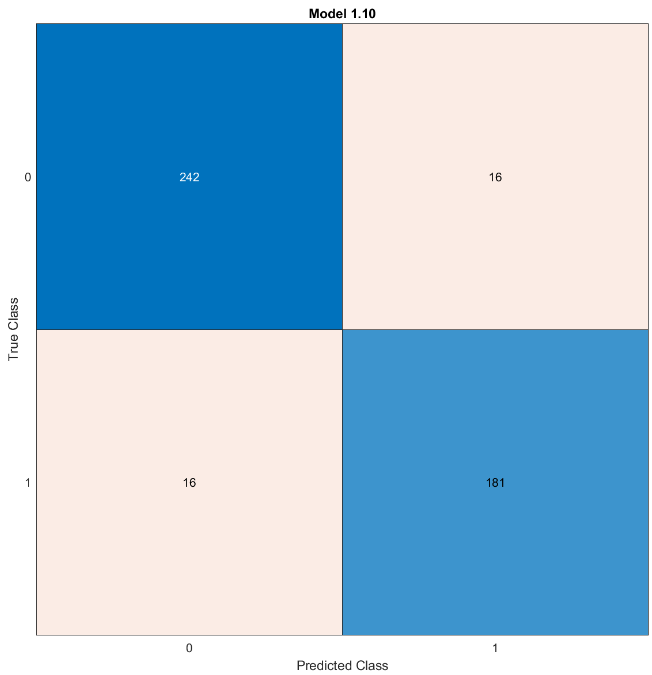

Figure 4.17: Confusion matrix for $R = 1$, $K = 8$, $d = 2$ for database 2 - RIM-ONE r2 after data pre-processing

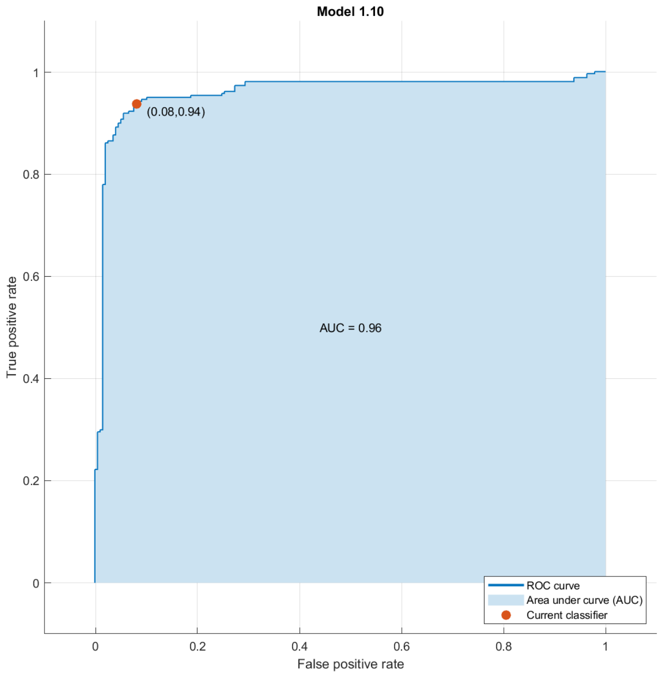

Figure 4.18: Receiver operating characteristic (ROC) for $R = 1$, $K = 8$, $d = 2$ for database 2 - RIM-ONE r2 after data pre-processing

4.5 Results for other local image descriptors

In Sections 4.3 and 4.4 we have seen the results for the LWP image descriptor as applied to two databases. In this section we will present the results of two more local descriptors namely the LBP and the LTP. These local image descriptors use the intensity values of the neighboring pixels directly without applying any wavelet decomposition and hence do not take into account the relationship that exists among the neighbors before comparison with the center pixel. As a result these image descriptors produce poorer feature vectors as compared to LWP and hence have lower classification accuracy.

4.5.1 LBP

The best results for LBP are as follows: We achieved an accuracy of 81.7% with the help of fine tree medium tree classifiers without applying data pre-processing. The results were obtained for the r1 database. The confusion matrix and the receiver operating characteristic (ROC) curve are shown in Figures. 4.19 and 4.20.

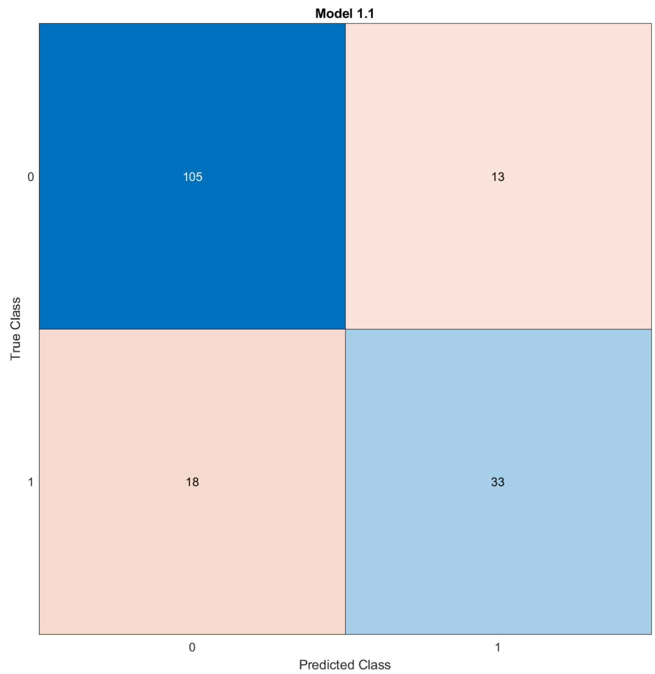

Figure 4.19: Confusion matrix for LBP before data pre-processing

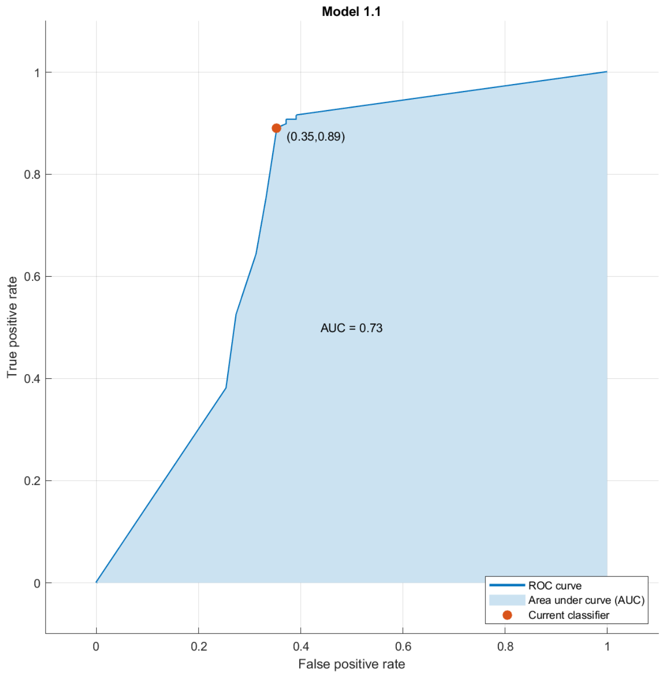

Figure 4.20: Receiver operating characteristic (ROC) for LBP before data pre-processing

An accuracy of 93.5% was obtained with the help of cubic SVM classifier after data pre-processing. The results were obtained for the r1 database. The confusion matrix and the receiver operating characteristic (ROC) curve are shown in Figures. 4.21 and 4.22.

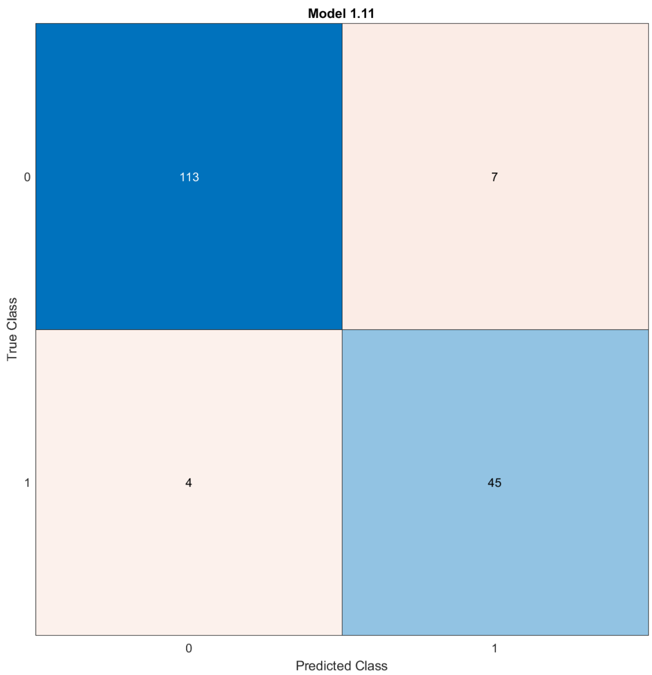

Figure 4.21: Confusion matrix for LBP after data pre-processing

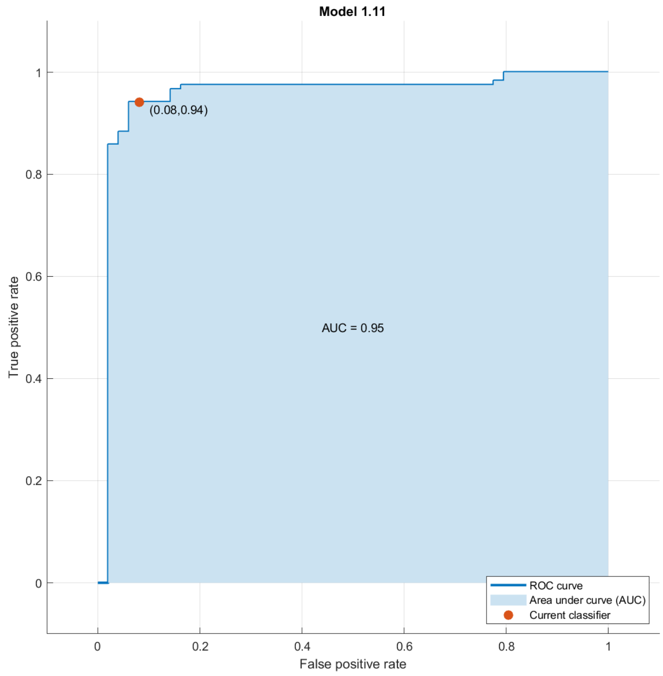

Figure 4.22: Receiver operating characteristic (ROC) for LBP after data pre-processing

4.5.2 LTP

The best results for LTP are as follows: We achieved an accuracy of 79.9% with the help of ensemble (bagged trees) classifier without applying data pre-processing. The results were obtained for the r1 database. The confusion matrix and the receiver operating characteristic (ROC) curve are shown in Figures. 4.23 and 4.24.

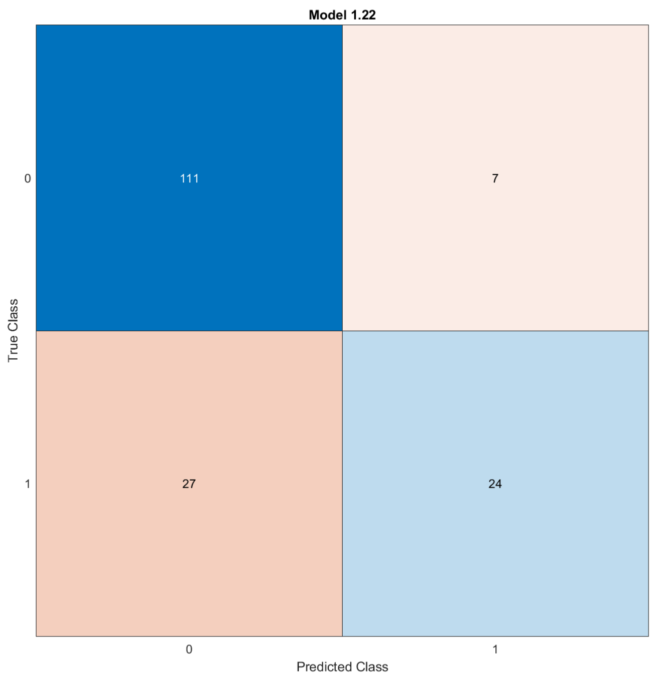

Figure 4.23: Confusion matrix for LTP before data pre-processing

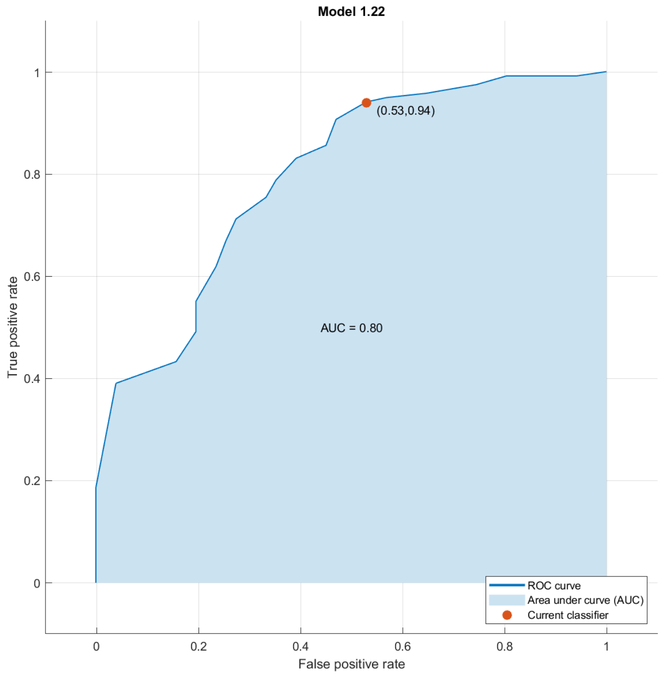

Figure 4.24: Receiver operating characteristic (ROC) for LTP before data pre-processing

An accuracy of 90.5% was obtained with the help of ensemble (bagged trees) classifier after data pre-processing. The results were obtained for the r1 database. The confusion matrix and the receiver operating characteristic (ROC) curve are shown in Figures. 4.25 and 4.26.

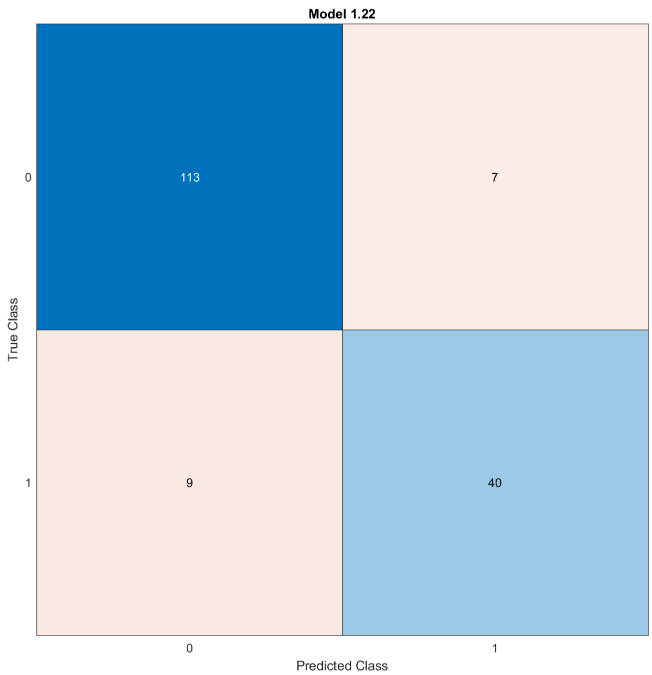

Figure 4.25: Confusion matrix for LTP after data pre-processing

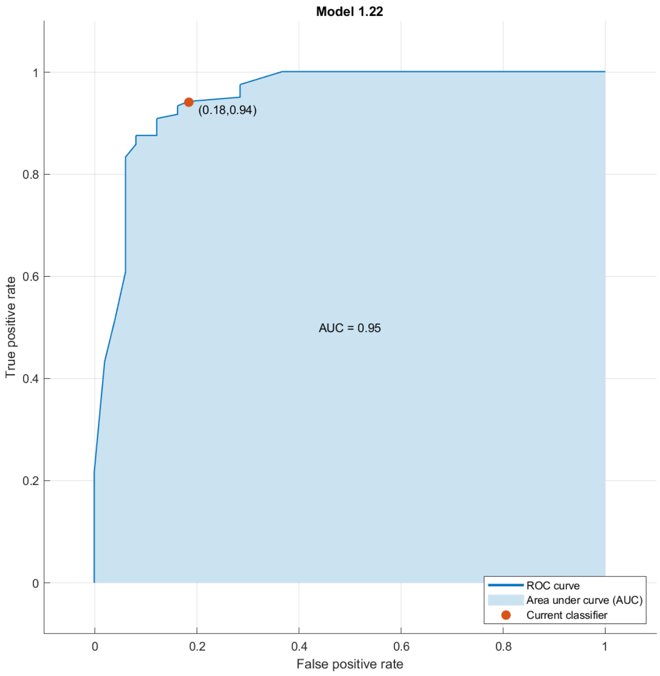

Figure 4.26: Receiver operating characteristic (ROC) for LTP after data pre-processing

Chapter 5

Conclusions and Future Work

5.1 Conclusion

The local wavelet pattern (LWP) image descriptor has been proposed in this thesis for the purpose of glaucoma detection. This image descriptor has the peculiar property that it considers the relationship that exists among the local neighbors of any center pixel before it is used for comparison with the center pixel. The LWP is computed for each and every pixel of the fundus image and finally the feature vector is developed for the entire image. We have applied the LWP image descriptor over two RIM-ONE databases (namely RIM-ONE r1 and RIM-ONE r2) and compared the results with two other local image descriptors name, the local binary pattern (LBP) and the local ternary pattern (LTP). The results show that the LWP outperforms other local image descriptors for glaucoma detection. Also the dimension of the LWP feature vector only depends on the number of local neighbors K considered and reduces the computational complexity drastically.

5.2 Future Work

The current version of the algorithm only considers glaucoma detection. The algorithm can be developed further in order to predict many other retinal diseases such as age-related macular degeneration, diabetic retinopathy, retinopathy of prematurity, and Stargardt's disease. Thus we can modify the algorithm to make it a multi-class classification problem.

Our algorithm takes into account the entire fundus image for image classification. In order to improve the accuracy of glaucoma detection we can incorporate an image segmentation stage in our algorithm to only consider the optic nerve head (ONH) region of the fundus image since changes in this region is the deciding factor in glaucoma diagnosis. This also greatly reduces the computational complexity involved in implementing the algorithm since only a portion of the image is being considered.

Also we can consider the recent option of applying Deep learning (DL) for glaucoma detection. With more and more fundus image datasets being made available publicly having large number of high resolution images, DL has become a viable option for medical image classification problems.

Bibliography

[1] M. C. V. Stella Mary, E. B. Rajsingh, and G. R. Naik, "Retinal fundus image analysis for diagnosis of glaucoma: A comprehensive survey," *IEEE Access*, vol. 4, pp. 4327–4354, 2016.

[2] M. D. Abràmoff, M. K. Garvin, and M. Sonka, "Retinal imaging and image analysis," *IEEE Reviews in Biomedical Engineering*, vol. 3, pp. 169–208, 2010.

[3] R. S. Harwerth and H. A. Quigley, "Visual field defects and retinal ganglion cell losses in patients with glaucoma," *Archives of Ophthalmology*, vol. 124, no. 6, pp. 853–859, 2006.

[4] I. Akram and A. Rubinstein, "Common retinal signs. an overview," *Optometry Today*, 2005.

[5] J. B. Jonas, J. Stürmer, K. I. Papastathopoulos, F. Meier-Gibbons, and A. Dichtl, "Optic disc size and optic nerve damage in normal pressure glaucoma.," *British Journal of Ophthalmology*, vol. 79, no. 12, pp. 1102–1105, 1995.

[6] Y. C. Tham, X. Li, T. Y. Wong, H. A. Quigley, T. Aung, and C. Y. Cheng, "Global prevalence of glaucoma and projections of glaucoma burden through 2040: A systematic review and meta-analysis," *Ophthalmology*, vol. 121, no. 11, pp. 2081–2090, 2014.

[7] H. A. Quigley and A. T. Broman, "The number of people with glaucoma worldwide in 2010 and 2020," *British Journal of Ophthalmology*, vol. 90, no. 3, pp. 262–267, 2006.

[8] L. S. Lim, P. Mitchell, J. M. Seddon, F. G. Holz, and T. Y. Wong, "Age-related macular degeneration," *The Lancet*, vol. 379, no. 9827, pp. 1728–1738, 2012.

[9] R. Klein, T. Peto, A. Bird, and M. R. Vannewkirk, "The epidemiology of age-related macular degeneration," *American Journal of Ophthalmology*, vol. 137, no. 3, pp. 486–495, 2004.

[10] C. L. Tsai, B. Madore, M. J. Leotta, M. Sofka, G. Yang, A. Majerovics, H. L. Tanenbaum, C. V. Stewart, and B. Roysam, "Automated retinal image analysis over the internet," *IEEE Transactions on Information Technology in Biomedicine*, vol. 12, no. 4, pp. 480–487, 2008.

[11] P. K. Chaudhary and R. B. Pachori, "Automatic diagnosis of glaucoma using two-dimensional Fourier-Bessel series expansion based empirical wavelet transform," *Biomedical Signal Processing and Control*, vol. 64, p. 102 237, 2021, ISSN: 1746-8094.

[12] R. B. Pachori and P. Sircar, "Analysis of multicomponent AM-FM signals using FB-DESA method," *Digital Signal Processing*, vol. 20, no. 1, pp. 42–62, 2010, ISSN: 1051-2004.

[13] J. Nayak, R. Acharya U., P. S. Bhat, N. Shetty, and T. C. Lim, "Automated diagnosis of glaucoma using digital fundus images," *Journal of Medical Systems*, vol. 33, no. 5, p. 337, Aug. 2008, ISSN: 1573-689X.

[14] A. Chakravarty and J. Sivaswamy, "Glaucoma classification with a fusion of segmentation and image-based features," in *2016 IEEE 13th International Symposium on Biomedical Imaging (ISBI)*, IEEE, 2016, pp. 689–692.

[15] R. Bock, J. Meier, L. G. Nyúl, J. Hornegger, and G. Michelson, "Glaucoma risk index: Automated glaucoma detection from color fundus images," *Medical Image Analysis*, vol. 14, no. 3, pp. 471–481, 2010, ISSN: 1361-8415.

[16] K. P. Noronha, U. R. Acharya, K. P. Nayak, R. J. Martis, and S. V. Bhandary, "Automated classification of glaucoma stages using higher order cumulant features," *Biomedical Signal Processing and Control*, vol. 10, pp. 174–183, 2014, ISSN: 1746-8094.

[17] R. Sharma, R. B. Pachori, and P. Sircar, "Seizures classification based on higher order statistics and deep neural network," *Biomedical Signal Processing and Control*, vol. 59, p. 101 921, 2020, ISSN: 1746-8094.

[18] U. R. Acharya, E. Ng, L. W. J. Eugene, K. P. Noronha, L. C. Min, K. P. Nayak, and S. V. Bhandary, "Decision support system for the glaucoma using gabor transformation," *Biomedical Signal Processing and Control*, vol. 15, pp. 18–26, 2015, ISSN: 1746-8094.

[19] U. Raghavendra, S. V. Bhandary, A. Gudigar, and U. R. Acharya, “Novel expert system for glaucoma identification using non-parametric spatial envelope energy spectrum with fundus images,” *Biocybernetics and Biomedical Engineering*, vol. 38, no. 1, pp. 170–180, 2018, ISSN: 0208-5216.

[20] S. Maheshwari, R. B. Pachori, V. Kanhangad, S. V. Bhandary, and U. R. Acharya, “Iterative variational mode decomposition based automated detection of glaucoma using fundus images,” *Computers in Biology and Medicine*, vol. 88, pp. 142–149, 2017, ISSN: 0010-4825.

[21] C. Raja and N. Gangatharan, “Glaucoma detection in fundal retinal images using trispectrum and complex wavelet-based features,” *European Journal of Scientific Research*, vol. 97, no. 1, pp. 159–171, 2013.

[22] Y. Xu, S. Lin, D. W. K. Wong, J. Liu, and D. Xu, “Efficient reconstruction-based optic cup localization for glaucoma screening,” in *International Conference on Medical Image Computing and Computer-Assisted Intervention*, Springer, 2013, pp. 445–452.

[23] C. Raja and N. Gangatharan, “Appropriate sub-band selection in wavelet packet decomposition for automated glaucoma diagnoses,” *International Journal of Automation and Computing*, vol. 12, no. 4, pp. 393–401, Aug. 2015, ISSN: 1751-8520.

[24] C. Raja and N. Gangatharan, “Optimal hyper analytic wavelet transform for glaucoma detection in fundal retinal images,” *Journal of Electrical Engineering and Technology*, vol. 10, no. 4, pp. 1899–1909, 2015.

[25] M. Kumar, R. B. Pachori, and U. R. Acharya, “Characterization of coronary artery disease using flexible analytic wavelet transform applied on ECG signals,” *Biomedical Signal Processing and Control*, vol. 31, pp. 301–308, 2017, ISSN: 1746-8094.

[26] ——, “Automated diagnosis of myocardial infarction ECG signals using sample entropy in flexible analytic wavelet transform framework,” *Entropy*, vol. 19, no. 9, 2017, ISSN: 1099-4300.

[27] ——, “An efficient automated technique for CAD diagnosis using flexible analytic wavelet transform and entropy features extracted from HRV signals,” *Expert Systems with Applications*, vol. 63, pp. 165–172, 2016, ISSN: 0957-4174.

[28] ——, “Automated diagnosis of atrial fibrillation ECG signals using entropy features extracted from flexible analytic wavelet transform,” *Biocybernetics and Biomedical Engineering*, vol. 38, no. 3, pp. 564–573, 2018, ISSN: 0208-5216.

[29] V. Gupta, T. Priya, A. K. Yadav, R. B. Pachori, and U. R. Acharya, "Automated detection of focal EEG signals using features extracted from flexible analytic wavelet transform," *Pattern Recognition Letters*, vol. 94, pp. 180–188, 2017, ISSN: 0167-8655.

[30] S. Maheshwari, R. B. Pachori, and U. R. Acharya, "Automated diagnosis of glaucoma using empirical wavelet transform and correntropy features extracted from fundus images," *IEEE Journal of Biomedical and Health Informatics*, vol. 21, no. 3, pp. 803–813, 2017.

[31] A. Bhattacharyya and R. B. Pachori, "A multivariate approach for patient-specific EEG seizure detection using empirical wavelet transform," *IEEE Transactions on Biomedical Engineering*, vol. 64, no. 9, pp. 2003–2015, 2017.

[32] A. Bhattacharyya, M. Sharma, R. B. Pachori, P. Sircar, and U. R. Acharya, "A novel approach for automated detection of focal EEG signals using empirical wavelet transform," *Neural Computing and Applications*, vol. 29, no. 8, pp. 47–57, Apr. 2018, ISSN: 1433-3058.

[33] T. Kausu, V. P. Gopi, K. A. Wahid, W. Doma, and S. I. Niwas, "Combination of clinical and multiresolution features for glaucoma detection and its classification using fundus images," *Biocybernetics and Biomedical Engineering*, vol. 38, no. 2, pp. 329–341, 2018, ISSN: 0208-5216.

[34] R. Sharma, R. B. Pachori, and U. R. Acharya, "An integrated index for the identification of focal electroencephalogram signals using discrete wavelet transform and entropy measures," *Entropy*, vol. 17, no. 8, pp. 5218–5240, 2015, ISSN: 1099-4300.

[35] M. Sharma, P. Sharma, R. B. Pachori, and U. R. Acharya, "Dual-tree complex wavelet transform-based features for automated alcoholism identification," *International Journal of Fuzzy Systems*, vol. 20, no. 4, pp. 1297–1308, Apr. 2018, ISSN: 2199-3211.

[36] R. Sharma, P. Sircar, R. Pachori, S. V. Bhandary, and U. R. Acharya, "Automated glaucoma detection using center slice of higher order statistics," *Journal of Mechanics in Medicine and Biology*, vol. 19, no. 1, 2019.

[37] S. Maheshwari, V. Kanhangad, R. B. Pachori, S. V. Bhandary, and U. R. Acharya, "Automated glaucoma diagnosis using bit-plane slicing and local binary pattern techniques," *Computers in Biology and Medicine*, vol. 105, pp. 72–80, 2019, ISSN: 0010-4825.

[38] A. K. Tiwari, R. B. Pachori, V. Kanhangad, and B. K. Panigrahi, “Automated diagnosis of epilepsy using key-point-based local binary pattern of EEG signals,” *IEEE Journal of Biomedical and Health Informatics*, vol. 21, no. 4, pp. 888–896, 2017.

[39] D. K. Agrawal, B. S. Kirar, and R. B. Pachori, “Automated glaucoma detection using quasi-bivariate variational mode decomposition from fundus images,” *IET Image Processing*, vol. 13, no. 13, pp. 2401–2408, 2019.

[40] A. Upadhyay and R. B. Pachori, “Instantaneous voiced/non-voiced detection in speech signals based on variational mode decomposition,” *Journal of the Franklin Institute*, vol. 352, no. 7, pp. 2679–2707, 2015, ISSN: 0016-0032.

[41] A. Upadhyay and R. Pachori, “Speech enhancement based on mEMD-VMD method,” *Electronics Letters*, vol. 53, no. 7, pp. 502–504, 2017.

[42] Z. Zhang, F. S. Yin, J. Liu, W. K. Wong, N. M. Tan, B. H. Lee, J. Cheng, and T. Y. Wong, “Origa-light: An online retinal fundus image database for glaucoma analysis and research,” in *2010 Annual International Conference of the IEEE Engineering in Medicine and Biology*, IEEE, 2010, pp. 3065–3068.

[43] V. Gulshan, L. Peng, M. Coram, M. C. Stumpe, D. Wu, A. Narayanaswamy, S. Venugopalan, K. Widner, T. Madams, J. Cuadros, R. Kim, R. Raman, P. C. Nelson, J. L. Mega, and D. R. Webster, “Development and validation of a deep learning algorithm for detection of diabetic retinopathy in retinal fundus photographs,” *JAMA - Journal of the American Medical Association*, vol. 316, no. 22, pp. 2402–2410, 2016.

[44] X. Chen, Y. Xu, S. Yan, D. W. K. Wong, T. Y. Wong, and J. Liu, “Automatic feature learning for glaucoma detection based on deep learning,” in *Medical Image Computing and Computer-Assisted Intervention – MICCAI 2015*, Cham: Springer International Publishing, 2015, pp. 669–677, ISBN: 978-3-319-24574-4.

[45] J. I. Orlando, E. Prokofyeva, M. del Fresno, and M. B. Blaschko, “Convolutional neural network transfer for automated glaucoma identification,” in *12th International Symposium on Medical Information Processing and Analysis*, SPIE, vol. 10160, 2017, pp. 241–250.

[46] R. K. Tripathy, A. Bhattacharyya, and R. B. Pachori, “Localization of myocardial infarction from multi-lead ECG signals using multiscale analysis and convolutional neural network,” *IEEE Sensors Journal*, vol. 19, no. 23, pp. 11 437–11 448, 2019.

[47] H. C. Shin, H. R. Roth, M. Gao, L. Lu, Z. Xu, I. Nogues, J. Yao, D. Mollura, and R. M. Summers, "Deep convolutional neural networks for computer-aided detection: CNN architectures, dataset characteristics and transfer learning," *IEEE Transactions on Medical Imaging*, vol. 35, no. 5, pp. 1285–1298, 2016.

[48] J. Martins, J. S. Cardoso, and F. Soares, "Offline computer-aided diagnosis for glaucoma detection using fundus images targeted at mobile devices," *Computer Methods and Programs in Biomedicine*, vol. 192, p. 105 341, 2020, ISSN: 0169-2607.

[49] F. Fumero, S. Alayon, J. L. Sanchez, J. Sigut, and M. Gonzalez-Hernandez, "RIM-ONE: An open retinal image database for optic nerve evaluation," in *2011 24th International Symposium on Computer-Based Medical Systems (CBMS)*, 2011, pp. 1–6.

[50] S. R. Dubey, S. K. Singh, and R. K. Singh, "Local wavelet pattern: A new feature descriptor for image retrieval in medical CT databases," *IEEE Transactions on Image Processing*, vol. 24, no. 12, pp. 5892–5903, 2015.

[51] P. K. Chaudhary and R. B. Pachori, "Automatic diagnosis of different grades of diabetic retinopathy and diabetic macular edema using 2d-fbse-fawt," *IEEE Transactions on Instrumentation and Measurement*, 2022.

[52] W. S. Noble, "What is a support vector machine?" *Nature Biotechnology*, vol. 24, no. 12, pp. 1565–1567, 2006.

[53] J. Laaksonen and E. Oja, "Classification with learning k-nearest neighbors," in *Proceedings of International Conference on Neural Networks (ICNN'96)*, IEEE, vol. 3, 1996, pp. 1480–1483.

[54] T. Hothorn and B. Lausen, "Bagging tree classifiers for laser scanning images: A data-and simulation-based strategy," *Artificial Intelligence in Medicine*, vol. 27, no. 1, pp. 65–79, 2003.

[55] R. E. Wright, "Logistic regression.," 1995.

[56] S. Chen and X. Yang, "Alternative linear discriminant classifier," *Pattern Recognition*, vol. 37, no. 7, pp. 1545–1547, 2004.